

# Investigation of Topographic Site Effects using 3D Waveform Modelling: Amplification, Polarization and Torsional Motions in the Case Study of Arquata del Tronto (Italy)

**Julie Baron**

Istituto Nazionale di Oceanografia e Geofisica Sperimentale

**Ilaria Primofiore**

Ministero dell'Istruzione, dell'Università e della Ricerca

**Peter Klin** (✉ [pklin@inogs.it](mailto:pklin@inogs.it))

Istituto Nazionale di Oceanografia e Geofisica Sperimentale <https://orcid.org/0000-0002-5373-4484>

**Giovanna Laurenzano**

Istituto Nazionale di Oceanografia e Geofisica Sperimentale

**Giovanna Vessia**

Università degli Studi Gabriele d'Annunzio Chieti Pescara

---

## Research Article

**Keywords:** Topographic amplification, directional site effect, torsional motion, numerical modeling, Arquata del Tronto, SPECFEM3D, cross-coupling of motion components in site response

**Posted Date:** June 4th, 2021

**DOI:** <https://doi.org/10.21203/rs.3.rs-582452/v1>

**License:**  This work is licensed under a Creative Commons Attribution 4.0 International License.

[Read Full License](#)

---

**Version of Record:** A version of this preprint was published at Bulletin of Earthquake Engineering on December 3rd, 2021. See the published version at <https://doi.org/10.1007/s10518-021-01270-2>.

1  
2  
3  
4  
5  
6  
7  
8  
9  
10  
11  
12  
13  
14  
15  
16  
17  
18  
19  
20  
21

# Investigation of topographic site effects using 3D waveform modelling: amplification, polarization and torsional motions in the case study of Arquata del Tronto (Italy)

Julie Baron<sup>1</sup>, Ilaria Primofiore<sup>2</sup>, Peter Klin<sup>1\*</sup>, Giovanna Vessia<sup>2</sup>, Giovanna Laurenzano<sup>1</sup>

<sup>1</sup> National Institute of Oceanography and Applied Geophysics - OGS, Borgo Grotta Gigante 42/C, 34010 Sgonico, Trieste, Italy

<sup>2</sup> University “G. d’ Annunzio” of Chieti-Pescara, Department of Engineering and Geology, Via dei Vestini 31, 66100 Chieti, Italy

\* Corresponding author. E-mail address: [pklin@inogs.it](mailto:pklin@inogs.it)

Julie Baron <https://orcid.org/0000-0002-3215-6996>

Ilaria Primofiore <https://orcid.org/0000-0002-5688-8067>

Peter Klin <https://orcid.org/0000-0002-5373-4484>

Giovanna Vessia <https://orcid.org/0000-0003-1733-7112>

Giovanna Laurenzano <https://orcid.org/0000-0002-2618-3007>

## 22 Abstract

23 The combined effect of topography and near-surface heterogeneities on the seismic response is hardly  
24 predictable and may lead to an aggravation of the ground motion. We apply physics-based numerical  
25 simulations of 3D seismic wave propagation to highlight these effects in the case study of Arquata del Tronto, a  
26 hamlet in the Apennines that suffered irregularly distributed damage during the 2016 seismic sequence in  
27 Central Italy. We analyze the linear visco-elastic seismic response for vertically incident plane waves in terms of  
28 spectral amplification, polarization and induced torsional motion within the frequency band 1-8 Hz over a 1  
29 km<sup>2</sup> square area, with spatial resolution 25 m. To discern the effects of topography from those of the sub-surface  
30 structure we iterate the numerical simulations for three different versions of the structural  
31 model: one homogeneous, one with a surficial weathering layer and a soil basin and one with a complex internal  
32 structure. The numerical results confirm the correlation between topographic curvature and amplification and  
33 support a correlation between the induced torsional motion and the topographic slope. On the other hand we find  
34 that polarization does not necessarily imply ground motion amplification. In the frequency band above 4 Hz the  
35 topography-related effects are mainly aggravated by the presence of the weathering layer, even though they do  
36 not exceed the soil-related effects in the flat-topography basin. The structure below the weathering layer plays a  
37 recognizable role in the topography-related site response only for frequencies below 4 Hz.

## 38 Keywords

39 Topographic amplification, directional site effect, torsional motion, numerical modeling, Arquata del Tronto,  
40 SPECFEM3D, cross-coupling of motion components in site response

## 41 Introduction

42 The estimation of ground motion amplification due to site effects plays a fundamental role in the efforts devoted  
43 to seismic-risk mitigation (Amanti et al. 2020). Thanks to ground motion recordings and earthquake damage  
44 reports from sites characterized by topography, it has long been known that topographic features are an indicator  
45 of site effects, but theoretical explanations based on the relief's geometrical characteristics usually  
46 underestimated the observed amplification values (Geli et al. 1988). The discrepancies between predictions and  
47 observations can be ascribed to the absence of adequate reference site in many experimental estimates  
48 (Pedersen et al. 1994; Wood and Cox 2016) on one hand, and on the other hand, to the adoption of  
49 oversimplified models in theoretical estimates. The oversimplification that may cause underestimation of  
50 theoretically predicted amplifications typically consists of inadequate two-dimensional (2D) approximation of  
51 prominently three-dimensional (3D) topographic features (Paolucci 2002; Luo et al. 2020) or in neglecting  
52 impedance contrasts in the subsurface structure that possibly concur with topography in forming amplification  
53 effects (Graizer 2009; Assimaki and Jeong 2013; Hailemikael et al. 2016, to cite a few).

54 There is today a general agreement that topography implies a number of effects, discussed in the overview  
55 provided by Massa et al. (2014) and briefly summarized in the points below:

- 56 • Amplification occurs at the top of the topographic high in the wavelength range comparable to the  
57 width of the morphological relief (peak frequency decreases with increasing relief width).
- 58 • Amplification is proportional to the shape ratio (height vs. base half-width) of the relief.
- 59 • Amplification is larger for horizontal components, in particular for the component transverse to the  
60 direction of elongation of the relief.
- 61 • Topographic amplification is dependent on the source-to-site direction, numerical results however  
62 indicate that it is maximized for waves with vertical incidence.
- 63 • Topographic effects combined with the effects of structural heterogeneities, give rise to *atypical*  
64 topographic effects.

65 In order to account for possible topography-related amplification effects, a number of international seismic  
66 codes (e.g. Eurocode 8, NTC18 in Italy) have introduced the topographic aggravation factor (TAF) based on  
67 approximate topographic descriptions. Recently the efforts are focused on the development of more  
68 sophisticated TAF estimators, based on the availability of digital elevation maps (DEM) and equivalent uniform  
69 rock stiffness estimates (Grelle et al. 2018). Zhou et al. (2020) adopt the back-propagation neural network  
70 technique for the derivation of a ground motion amplification model based on topographic geometrical features  
71 estimated from the DEM. Since they are based on surface topography alone, these approaches neglect possible  
72 interactions between topographic and structural effects on wave propagation. According to Burjánek et al.  
73 (2014), the observed amplification at sites with comparable topography but with different subsurface structure  
74 may differ for a factor which is significantly larger than the expected ground motion variability and studies  
75 based exclusively on the terrain topography have almost no chance to capture the site effects correctly.

76 In the present work we address the problem of possible ground motion aggravation due to the complex  
77 interaction between a pronounced topographic relief and a heterogeneous distribution of underground seismic  
78 velocities. Given that the distinction of topographic effects from the stratigraphic ones in the seismic records  
79 results impractical, we adopted an approach that fully relies on numerical simulations to separate the two  
80 (Ashford et al. 1997). Three-dimensional (3D) physics-based numerical simulations of seismic wave  
81 propagation can provide a detailed and accurate characterization of the seismic ground motion and allow us to  
82 explore its spatial heterogeneity. This kind of numerical simulations have proven to be essential for the  
83 explanation of anomalies in the observed ground motion during past earthquakes (e. g. Paolucci et al. 2015;  
84 Cruz-Atienza et al. 2016; Klin et al. 2019), also in cases in which topographic effects are involved (e.g. Puglia et  
85 al. 2013; Luo et al. 2020). Moreover, numerical simulations allow the quantification of potential amplification  
86 effects at sites where ground motion data is lacking (e. g. Fehr et al. 2019).

87 In the present work we analyze the site response not only in the conventional terms of spectral amplification but  
88 also in terms of induced polarization and induced rotations in the horizontal components of ground motion.  
89 According to several works (e. g. Burjánek et al. 2014; Massa et al. 2014; Pischiutta et al. 2018), the  
90 polarization of the site response can be viewed as an indicator of topography-induced strong site effects, even  
91 though the direction of polarization is not strictly related with the main directions of the topographic features.  
92 Given that the polarization of the site response can be identified by low-cost single-station analyses, deepening  
93 this topic could provide useful indications for micro-zonation studies.

94 On the other hand, ground motion rotations are rarely considered in site effects studies, due to difficulties  
95 involved in measuring rotational motions and strains and because of a widespread preconception in the  
96 seismological community that rotational motions are insignificant (Lee et al. 2009). In the earthquake  
97 engineering community instead, the ground rotational motion gained interest (Lee and Trifunac 1985; Castellani  
98 et al. 2012), since the *travelling wave effect* was recognized by Newmark (1969) and it is today accounted for in  
99 building codes under the term *accidental eccentricity* (Anagnostopoulos et al. 2015). While the research  
100 regarding the relevance of ground motion rotations is still undergoing (Guidotti et al. 2018), in the present work  
101 we investigate the possibility of topography-induced rotations around the vertical axis (torsional motion).  
102 Topography-related torsional motions were observed - without a quantitative analysis - by Stupazzini et al.  
103 (2009) in their 3D numerical simulations of earthquake ground motion in the Grenoble valley. In the present  
104 work we set up a simple predictive model which relates torsional motions and the topographic slope in  
105 homogeneous media and we evaluate the possible variations due to near surface heterogeneities.

106 We elected as case study for the aforementioned investigations the 1 km<sup>2</sup> square area centered in the historical  
107 center of Arquata del Tronto, a village in the Central Apennines located on an elongated WNW-ESE ridge at an  
108 elevation of about 100 meters above the underlying valley. The village suffered extensive damage and collapses  
109 in the 2016 August 24<sup>th</sup> Mw 6.0 Amatrice earthquake and the non-uniform damage distribution indicated  
110 possible topography-related site effects (Galli et al. 2016; Lanzo et al. 2019). An evaluation of site effects in  
111 Arquata del Tronto and Borgo from seismological data has been performed by Laurenzano et al. (2019), who  
112 exploited earthquake recordings acquired on temporary seismic stations deployed after the first mainshock of  
113 the 2016 seismic sequence. Their study evidenced a substantial difference between the frequency-dependent site  
114 amplification function at a location on the top of the ridge and in the valley below. A directional effect that  
115 could be associated to the ridge orientation has been pointed out, as well. In order to quantitatively explain the  
116 observed site response characteristics, Giallini et al. (2020) applied 2D numerical simulations using subsoil  
117 models deduced from the available geognostic, geophysical and geomechanical surveys and evidenced the  
118 coupling effect of stratigraphy and topography associated with the presence of a weathered portion of the rock  
119 mass and the alternation of highly dipping rocky materials. They admitted that 2D analyses cannot fully capture  
120 the behavior of such an asymmetric ridge and suggested for this site tridimensional numerical analyses. This  
121 origin of the site effects was finally verified by Primofiore et al. (2020), who set up an updated 3D digital model  
122 of the area and evaluated the resulting ground motion by means of 3D numerical simulations of seismic wave  
123 propagation.

124 The present work can be therefore considered as a follow up of the analyses by Primofiore et al. (2020). In order  
125 to provide general results and some new insights with respect to the topography-related site effects, we iterate  
126 the numerical evaluation of ground motion for three different versions of the Arquata del Tronto visco-elastic  
127 structural model, with growing complexity. The first version is characterized by a homogeneous structure, the  
128 second one presents near surface alterations (weathering layer and a restricted soil basin over a flat area), and  
129 the third one exhibits a complex internal structure and corresponds to the one used in Primofiore et al. (2020).  
130 The differences between the seismic responses evaluated for each model are then measured in terms of the effect  
131 size in three different frequency bands of engineering interest. We also analyze the possible correlation between  
132 the amplification and the topographic curvature, which was proposed as a proxy for topographic amplification  
133 by Maufroy et al. (2015).

134

## 135 Method

### 136 Description of site response in terms of response function 3 × 3 matrix

137 In our characterization of site effects we follow Paolucci (1999) and employ 3D impulse response functions  
138 evaluated from 3D physics-based numerical simulations of seismic wave propagation. The 3D response function  
139 consists of a 3×3 matrix with components  $h_{ij}(\mathbf{x}, t)$ . The time series  $h_{ij}(\mathbf{x}, t)$  describes the  $i$ -th spatial component  
140 of the seismic time series that is observed at the site  $\mathbf{x}$  when the area is investigated by a vertically incident  
141 impulsive plane wave polarized in the  $j$ -th direction with unitary amplitude. We can express the ground motion  
142  $\mathbf{y}(\mathbf{x}, t) = [y_1(\mathbf{x}, t), y_2(\mathbf{x}, t), y_3(\mathbf{x}, t)]$  at the site  $\mathbf{x}$  for any vertically incident seismic input  $\mathbf{u}(t) = [u_1(t), u_2(t), u_3(t)]$  as  
143

$$144 \quad y_i(\mathbf{x}, t) = \sum_j h_{ij}(\mathbf{x}, t) * u_j(t) \quad 1)$$

145 where  $*$  denotes convolution in time. In virtue of the convolution theorem, the expression can be evaluated as a  
146 multiplication in the frequency domain  
147

$$148 \quad Y_i(\mathbf{x}, f) = \sum_j H_{ij}(\mathbf{x}, f) U_j(f) \quad 2)$$

149 where we denote with uppercase letters the Fourier spectrum of the corresponding time-domain quantities  
150 denoted in lowercase letters.  
151

152 If an ideal elastic medium was considered, we could numerically evaluate the terms  $h_{ij}(\mathbf{x}, t)$  as the three  
153 component solutions of the wave field at the topographic surface for three cases of unitary impulsive plane wave  
154 entering the spatial domain from below. In the present case however, a viscoelastic medium is considered and  
155 the intrinsic attenuation (and dispersion) would imply a response function which is dependent on the depth at  
156 which the plane wave is excited. In order to get rid of this incongruence, we adopted a redefinition of 3D  
157 response functions based on the concept of the reference site. In this approach, we evaluate the solutions for  
158 polarized plane waves also in a “reference” spatial domain, characterized by a homogeneous medium (having  
159 the properties of the bedrock in the geomodel under investigation) and flat topographic surface (with elevation  
160 equal to the average of the studied case). The depth at which the plane wave is introduced is irrelevant, as long  
161 as it is the same in the two cases. If we denote the frequency domain solutions in the reference medium and in  
162 the investigated medium with  $U_{ij}^{ref}$  and  $U_{ij}$  respectively, (with the index  $i$  denoting the spatial component of the  
163 solution and the index  $j$  denoting the polarization of the excited plane wave) we can estimate the components of  
164 the response function of the geomodel under investigation in frequency domain as the quotients  
165

$$166 \quad \begin{aligned} H_{11} &= \frac{U_{11}}{U_{11}^{ref}}; & H_{12} &= \frac{U_{12}}{U_{22}^{ref}}; & H_{13} &= \frac{U_{13}}{U_{33}^{ref}}; \\ H_{21} &= \frac{U_{21}}{U_{11}^{ref}}; & H_{22} &= \frac{U_{22}}{U_{22}^{ref}}; & H_{23} &= \frac{U_{23}}{U_{33}^{ref}}; \\ H_{31} &= \frac{U_{31}}{U_{11}^{ref}}; & H_{32} &= \frac{U_{32}}{U_{22}^{ref}}; & H_{33} &= \frac{U_{33}}{U_{33}^{ref}}. \end{aligned} \quad 3)$$

167 This definition of the response functions also relaxes the request of the unitary and impulsive character of the  
168 plane wave entering the spatial domain and permits the adoption of a time function which suits at best the  
169 numerical method we use in the simulations.  
170

### 171 Computation of response function from 3D model with SPEC3D

172 Fundamental factors for a successful numerical simulation consist in the availability of a plausible 3D structural  
173 model of the spatial domain with an adequate geophysical characterization of the geological formations and in  
174 the accurate application of a numerical method for the solution of the elastodynamic wave equation.  
175

176 In the present work, we constructed a digital 3D structural model of the studied area by means of the  
177 commercial software Geomodeler3D, which interpolates the available geological data with methods based on  
178 the compliance of stratigraphic rules and on the interpretation of geologic surfaces as isopotential surfaces of a  
179 scalar potential field (Calcagno et al. 2008). We considered the geological and geophysical data from the  
180 surveys performed in the area during microzonation studies (ISPRA 2018; Puzzilli et al. 2019). Details on the  
181 3D model we built are discussed in section Models.

182 Considering the need to solve accurately the wave propagation in a spatial domain bounded by an irregularly  
183 shaped free surface, we decided to perform the numerical simulations with the Spectral Element Method (SEM).

184 This approach, first introduced in the study of acoustic and elastic waves by Seriani and Priolo (1994), combines  
 185 the geometrical flexibility of Finite Elements Methods (FEM) with the accuracy of the spectral methods. In  
 186 order to perform the simulations presented in the present work, we relied on the software SPEC3D  
 187 Cartesian from source (Peter et al. 2011). The code accounts for the intrinsic attenuation properties of the  
 188 viscoelastic medium by means of a series of standard linear solid elements (Savage et al. 2010) and avoids the  
 189 boundary reflection artefacts thanks to the usage of the perfectly matched layer technique (Xie et al. 2014).

190

### 191 **Reduction of the 3x3 response function to the plane wave amplification function**

192 In seismic hazard studies the site effects are typically described as the ratio between the Fourier Amplitude  
 193 Spectrum (FAS)  $|Y_{hor}(x, f)|$  of the combined horizontal components of the ground motion at the observation site  $x$   
 194 and that of the seismic input  $|U_{hor}(f)|$

$$195 \quad A(x, f) = \frac{|Y_{hor}(x, f)|}{|U_{hor}(f)|} \quad 4)$$

196 where, having assumed that components 1 and 2 lay in the horizontal plane, we put

$$197 \quad |Y_{hor}(x, f)| = \frac{1}{\sqrt{2}} \sqrt{|Y_1(x, f)|^2 + |Y_2(x, f)|^2} \quad 5)$$

198 and an analogous expression for  $|U_{hor}(f)|$ .

199 According to equation (2), the horizontal components of the ground motion at the observation site depend also  
 200 on the vertical components of the seismic input, which are not accounted for in the denominator of the spectral  
 201 ratio defined in equation (4). Since the vertical component of the seismic input is not uniquely determined by the  
 202 horizontal components, in our construction the amplification  $A(x, f)$  behaves as a random variable. Since we can  
 203 expect a log-normal distribution for the spectral amplitude ratios  $A_n(x, f)$  corresponding to different seismic  
 204 inputs denoted by the index  $n$ , the most efficient choice for their characterization are the geometric average  
 205  $\bar{A}^*(x, f)$  and the *multiplicative* or *geometric* standard deviation (GSD)  $\sigma^*(x, f)$  defined as

$$206 \quad \bar{A}^*(x, f) = \exp(\bar{A}_{ln}) \quad \text{where} \quad \bar{A}_{ln} = \frac{1}{N} \sum_{n=1}^N \ln(A_n(x, f));$$

$$\sigma^*(x, f) = \exp(\sigma_{ln}) \quad \text{where} \quad \sigma_{ln} = \left( \frac{1}{N-1} \sum_{n=1}^N (\ln(A_n(x, f)) - \bar{A}_{ln})^2 \right)^{1/2}. \quad 6)$$

207

208 In this study we estimate the site average amplification and its multiplicative standard deviation by considering  
 209 a set of three component earthquake ground motion records as seismic inputs  $U^{(n)}(f)$  and by evaluating the  
 210 correspondent theoretical site recordings  $Y^{(n)}(x, f)$  by applying eq. (2). Since we consider the numerical solutions  
 211 for vertically emerging plane waves, we call this estimation of the site amplification as plane-wave  
 212 amplification. The reduction of the 3x3 response function to the site amplification function can be therefore  
 213 obtained by replacing in equation (6) the terms

$$214 \quad A_n = \sqrt{\frac{|H_{11}U_1^{(n)} + H_{12}U_2^{(n)} + H_{13}U_3^{(n)}|^2 + |H_{21}U_1^{(n)} + H_{22}U_2^{(n)} + H_{23}U_3^{(n)}|^2}{|U_1^{(n)}|^2 + |U_2^{(n)}|^2}} \quad 7)$$

215 where  $H_i$  are 3D response functions as defined in equation (3) and where we omit the frequency and space  
 216 dependence from the notation for the sake of simplicity.

217 In the present analysis we considered as seismic inputs the ground motion records of 200 events with magnitude  
 218 in the range from  $M=2.8$  to  $M=4.8$  that occurred during the 2016-17 Amatrice seismic sequence (see Figs. S1  
 219 and S2 in supplemental information) and that were collected at the reference site station MZ75 on geological  
 220 bedrock at Montegallo municipality, 9 km north of Arquata del Tronto (Laurenzano et al. 2019). The GSD  
 221 considered in the results therefore depicts the amplification function's uncertainty, that is due to the variable  
 222 contribution of the input motion's vertical component to the output motion's horizontal components through the  
 223 cross-coupling effects (Paolucci 1999).

224

### 225 **Horizontal polarization analysis from the 3x3 response function**

226 Site effects on pronounced reliefs are usually correlated with ground motion directionality (Burjánek et al. 2014;  
 227 Massa et al. 2014) and a polarization analysis of the site response is therefore appropriate. We limit our  
 228 polarization analysis to the horizontal components and following the scheme of the plane wave amplification

229 analysis we define the plane wave directional amplification  $\bar{A}_\varphi^*(x, f)$  as the geometric average of the ratio of the  
 230 FAS of the ground motion component in the direction  $\varphi$  measured clockwise from the 2nd axis (North) and the  
 231 FAS of the seismic input in the same direction

$$232 \quad \bar{A}_\varphi^*(x, f) = \exp\left(\frac{1}{N} \sum_{n=1}^N \ln \frac{|Y_\varphi^{(n)}|}{|U_\varphi^{(n)}|}\right). \quad 8)$$

233  
 234 The amplitude spectra of the seismic motion  $|S(f)|$  in direction  $\varphi$  is evaluated from the complex spectra of the  
 235 two horizontal components  $S_1(f)$  and  $S_2(f)$  as

$$236 \quad |S_\varphi| = |S_1 \sin \varphi + S_2 \cos \varphi|. \quad 9)$$

237  
 238 In particular, we set  $S_1=U_1^{(n)}$  and  $S_2=U_2^{(n)}$  when evaluating  $|U_\varphi^{(n)}|$  whereas  $S_1=H_{11}U_1^{(n)} + H_{12}U_2^{(n)} + H_{13}U_3^{(n)}$  and  
 239  $S_2=H_{21}U_1^{(n)} + H_{22}U_2^{(n)} + H_{23}U_3^{(n)}$  when evaluating  $|Y_\varphi^{(n)}|$ . The polarization analysis consists in the computation of  
 240 the directional amplification function for azimuth angles from  $0^\circ$  to  $175^\circ$  using a  $5^\circ$  step.

### 241 242 **Rotation rate analysis from the 3x3 response function**

243 In consideration of the growing interest for the implications of the differential ground motion in seismic hazard  
 244 (Guidotti et al. 2018), we attempted to analyze how topography and structure-topography interaction may  
 245 induce torsional excitation (i.e., rotation around the vertical axis) at the Arquata del Tronto site. Given the  
 246 ground velocity time series  $\nu(\mathbf{x}, t)=[v_1(\mathbf{x}, t), v_2(\mathbf{x}, t), v_3(\mathbf{x}, t)]$  in a grid of points  $\mathbf{x}$  at surface, we follow the notation  
 247 suggested in Evans and IWGoRS (2009) and describe the rotation around the vertical axis by means of the  
 248 rotation rate

$$249 \quad \dot{\theta}_3(t) = \frac{1}{2} \left( \frac{dv_2}{dx_1} - \frac{dv_1}{dx_2} \right). \quad 10)$$

250  
 251 In the case the ground motion is due to the passage of a plane wave, we can infer from equation (10) a  
 252 proportionality between the rotational motion and the time derivative of the translational motion (Newmark  
 253 1969). If we denote with  $\dot{\theta}_3(f)$  the Fourier spectrum of the rotation rate around the vertical axis and with  $\ddot{U}(f)$   
 254 the acceleration spectrum, we can write

$$255 \quad |\dot{\theta}_3(f)| = \frac{s}{2} |\ddot{U}(f)|, \quad 11)$$

256  
 257 where  $s$  denotes the horizontal slowness, i.e. the inverse of the apparent horizontal phase velocity of the  
 258 propagating wave. The validity of equation (11) and of its equivalent in terms of peak ground rotation and peak  
 259 horizontal velocity has been confirmed in field observations (e.g. Spudich and Fletcher 2008) and reproduced in  
 260 numerical simulations (e.g. Stupazzini et al. 2009) in topography-free cases. Here we discuss instead the  
 261 implications of equation (11) in the case of topographic features for a vertically emerging plane wave.  
 262 A vertically emerging plane wave in a homogeneous medium with horizontal flat surface is characterized by  $s=0$   
 263 and thus implies no rotation. On the other hand, heterogeneities and topographic features would imply local  
 264 variations of  $s$  and consequently may induce torsional motion as a site effect. Simple geometrical considerations  
 265 allow us to deduce that in the ideal case of a homogeneous elastic medium with shear wave velocity  $V_s$ , the  
 266 topographic surface with slope  $\beta$  would imply for a vertically emerging plane wave an apparent horizontal  
 267 slowness with value

$$268 \quad s = \frac{\tan \beta}{V_s}. \quad 12)$$

269  
 270 If we substitute eq. (12) in eq. (11) we can predict the local (i.e., dependent on the position  $\mathbf{x}$ ) scaling factor  $A_\theta$   
 271 between the Fourier amplitude spectra of the rotation rate and the acceleration of the seismic input as

$$272 \quad A_\theta = \frac{|\dot{\theta}_3|}{|\ddot{U}|} = \frac{\tan \beta}{2V_s}. \quad 13)$$

273  
 274 In the case of a layered medium, we can approximate  $V_s$  in eq. (13) with the weighted harmonic mean of  $V_s$  in  
 275 the uppermost layers, but we have to expect a larger dispersion of the effective scaling factor in respect of the  
 276 predicted one.

281 In order to evaluate the effectiveness of equation (13) in the case of our 3D models, we apply eq. (10) to  
 282 compute the rotation rate time series  $\dot{\theta}_3^{(n)}(t)$  from the horizontal components  $y_1^{(n)}(\mathbf{x}, t)$  and  $y_2^{(n)}(\mathbf{x}, t)$  of the ground  
 283 velocity on the topographic surface, that are in turn estimated from the  $n$ -th seismic input using eq. (1). Finally,  
 284 we evaluate the plane wave torsional scaling factor  $\bar{A}_\theta^*$  as the geometric average of the ratio between the Fourier  
 285 amplitude spectra of the rotation rate and of the horizontal acceleration of the seismic input  
 286

$$287 \quad \bar{A}_\theta^*(x, f) = \exp\left(\frac{1}{N} \sum_{n=1}^N \ln\left(\frac{|\dot{\theta}_3^{(n)}(x, f)|}{|\ddot{U}^{(n)}(f)|}\right)\right) \quad 14)$$

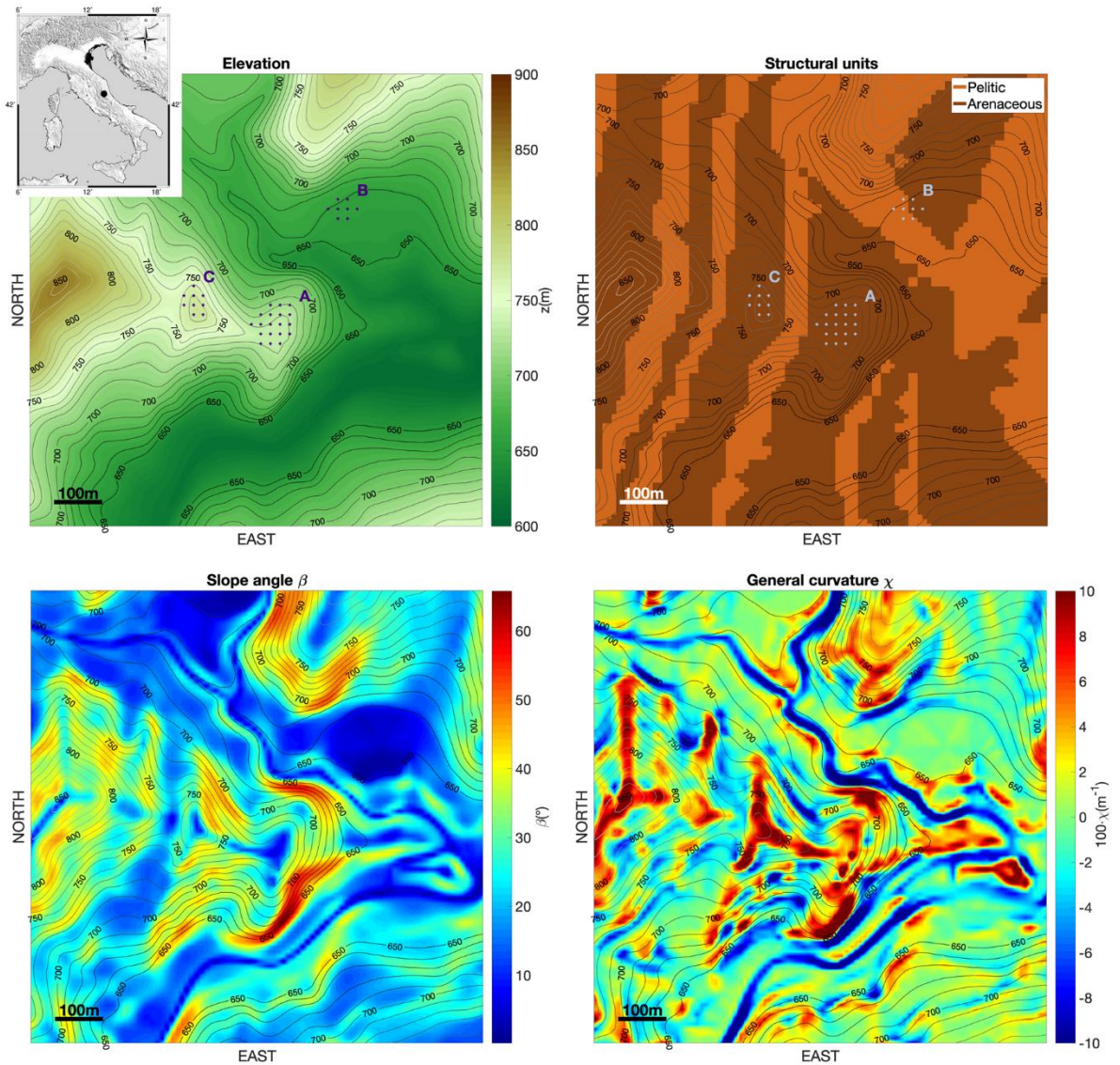
288 and the corresponding multiplicative standard deviation, in analogy with the amplification function.  
 289  
 290

## 291 The case study

292 We used numerical modeling to estimate the site response in a dense grid of points distributed over a limited area  
 293 centered on the location of the Arquata del Tronto village in Central Apennines (Italy).  
 294

### 295 **Geomorphological and lithological characters**

296 The geological substratum of the area is represented by the torbiditic member of the Laga formation consisting in  
 297 an alternation of Arenaceous and Pelitic-Arenaceous lithofacies (Giallini et al. 2020; Amanti et al. 2020). The  
 298 Laga formation is locally covered by fluvial deposits or arenaceous/calcareous debris (NE and SE area at the base  
 299 of the Arquata crest) and is characterized by the alternation of stratified, and roughly 50° WNW dipping, different  
 300 lithotypes belonging to the Laga formation. Instead, the substratum of Borgo in the valley below the hill presents  
 301 10 to 30 meters thick gravel deposits. In the description of the deep structure of the velocity model we consider  
 302 two units (i.e. the pelitic and the arenaceous unit), whereas other two units are considered to describe the overall  
 303 superficial 20 m thick alteration layer and the gravel deposits at Borgo. Further details regarding the set-up of the  
 304 3D geological model are given in Primofiore et al. (2020). We illustrate the morphological and lithological  
 305 characteristics of the area with the four maps in Fig. 1.



306 **Fig.1** topographic and morphologic characterization of the studied area. The location of the area in the Italian  
 307 peninsula is evidenced with the black dot in the small map overlapping the elevation map (upper left). The cross  
 308 marks in the elevation map indicate the virtual seismic stations in three sites of interest: site A corresponds to  
 309 Arquata del Tronto hamlet, site B to Borgo in the valley and Site C to the Castle promontory. In the structural  
 310 model map (upper right) we depict the alternance of pelitic and arenaceous formations just below the weathering  
 311 layer. The topographic slope and curvature are shown in the bottom left and right maps respectively  
 312  
 313

314 The elevation map evidences how the WNW-ESE oriented ridge of Arquata is transversely cut by saddles. The  
 315 elevation stands in a range between 600 and 860 m a.s.l. In the structural units map we represent the distribution  
 316 of the two deep structural units below the overall top alteration layer. In the same map we evidence the location  
 317 of three sites of particular interest: Site A corresponds to the Arquata historical city center, Site B corresponds to  
 318 the Borgo area in the valley and Site C corresponds to the Castle settlement on the crest. Site A and C are both  
 319 placed on the Arquata ridge and lay above the same arenaceous formation, whereas site B, in the valley, mostly  
 320 lays on the pelitic association with lower velocity (the gravel deposits that characterize site B are not shown in  
 321 the map). The other two maps show the distribution of the topography's slope and general curvature. If we  
 322 locally approximate the elevation  $z(x,y)$  with the polynomial (Zevenbergen and Thorne 1987):  
 323

$$z(x,y) = Ax^2y^2 + Bx^2y + Cxy^2 + Dx^2 + Ey^2 + Fxy + Gx + Hy + I, \quad (15)$$

324  
 325  
 326 The slope  $\beta$  and the general curvature  $\chi$  are defined (Moore et al. 1991)  
 327

328 
$$\beta = \tan^{-1} \sqrt{G^2 + H^2}; \quad \chi = -2(E + D) \quad 16)$$

329  
 330 The general curvature can be used as a general measure of the land convexity, in the sense that the positive  
 331 values indicate the convex surfaces (ridges and peaks), and the negative values identify concave surfaces, i.e.  
 332 valleys.

333 The steepest slopes of the ridge are found on the East and North sides of the promontory with a slope angle of 60  
 334 degree, whereas we can identify the area of high convexity with the main WNW-ESE ridge and its NS oriented  
 335 secondary ridges. Confronting the structural units map and the general curvature map, we observe that the NS  
 336 oriented secondary ridges overlap the outcrop of the arenaceous formation.

337  
 338  
 339 **Numerical models**

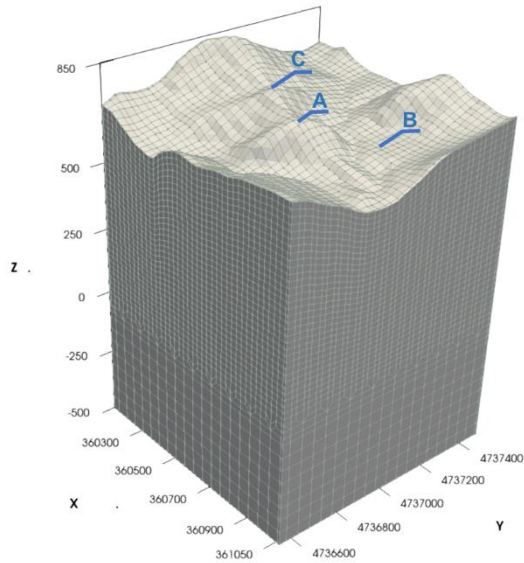
340 We simulated the wave propagation in a spatial domain that represents a square area centered on the Arquata del  
 341 Tronto hill, with 1 km long sides oriented along the geographical axes and that extends almost 1 km in depth.  
 342 Computer-aided 3D geological modeling allowed us to partition the domain in four main structural units (Table  
 343 1, AdT2 model), consistently with the geological map and a number of geological vertical sections (ISPRA 2018).

344  
 345 **Table 1** the structural units and their properties in the three geophysical models used for numerical simulations

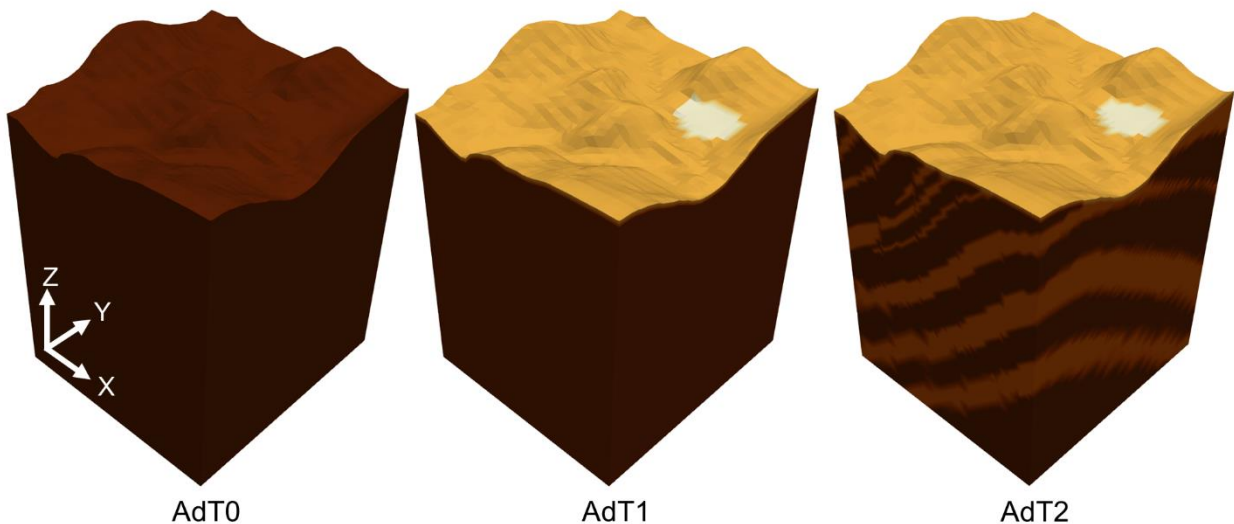
Model	Geological formation	Thickness (m)	Vs (m/s)	Vp (m/s)	Q $\mu$	Q $\kappa$	$\rho$ (kg/m <sup>3</sup> )
AdT0	Bedrock	-	1000	2480	100	350	2187
AdT1	Alluvial deposits	25	450	1116	45	157	1792
	Weathering layer	25	700	1736	70	245	2001
	Bedrock	-	1000	2480	100	350	2187
AdT2	Alluvial deposits	25	450	1116	45	157	1792
	Weathering layer	25	700	1736	70	245	2001
	Pelitic association	-	900	2232	90	315	2135
	Arenaceous association	-	1000	2480	100	350	2187

346  
 347  
 348 In order to perform the numerical simulations we embedded the described 3D domain in a larger volume with 3  
 349 km long side square base aligned with the cardinal directions, extending from a depth of 500 m b.s.l. to the top  
 350 surface which honors the 10 m resolution DEM Tinality (Tarquini et al. 2007). We discretized the spatial domain  
 351 with an unstructured mesh, made of 518.400 hexahedral elements, using the SPECFEM3D internal mesher. We  
 352 assigned to each element of the mesh the physical properties corresponding to the structural unit in its position.  
 353 The elements' size is approximately 25 m near the top of the volume, where the low seismic velocities that  
 354 characterize the alteration layer and alluvial deposits imply shorter wavelengths. On the other hand, we set an  
 355 element size of 50 m in the lower part of the volume, where seismic velocities are higher. A 75 m thick Perfectly  
 356 Matched Layer was applied on the lateral and bottom boundaries of the volume in order to exclude artefact  
 357 reflections from the numerical solution. The numerical mesh, clipped on the central 1 km<sup>2</sup> study area is presented  
 358 in Figure 2.

359 To investigate the separate contribution of stratigraphic and topographic effects on the seismic ground motion, we  
 360 carried out our analysis on three different geophysical models (Table 1 and Figure 3): AdT0, AdT1 and AdT2.  
 361 AdT0 presents a homogeneous structure and is therefore characterized by topographic effects alone. AdT1  
 362 includes a 25 m thick weathering layer below the surface and the alluvial deposits in the small basin at site B  
 363 whereas AdT2 includes also the distinction between the arenaceous and pelitic associations in the deeper structure.



364  
 365 **Fig.2** the central portion of the numerical mesh used for numerical simulations. The locations of the sites A, B  
 366 and C are shown. Length units are in meters, x-direction is eastward  
 367



368  
 369 **Fig.3** representation of the three input models clipped on the 1 km<sup>2</sup> square area of interest. AdT0 is the  
 370 homogeneous model, AdT1 is the homogeneous model with a weathering layer and an alluvial, AdT2 is the full  
 371 3D model of Arquata del Tronto retrieved from Primofiore et al. (2020)  
 372

373 We modelled the vertically incident plane waves by placing a horizontal carpet of sources at -400m a.s.l, with an  
 374 explosive mechanism for the vertically polarized plane wave and West-East or North-South oriented double  
 375 couple mechanism for the two independent cases of horizontally polarized plane waves, respectively. A set of  
 376 three simulations is therefore necessary to fully define the 3D response function. We performed simulations that  
 377 returned 8 s long three-component time series at 2304 points of the computational mesh in the central square  
 378 area of the topographic surface.

379 Considering the values of the mechanical properties (Table 1), the dimensions of the mesh elements imply a  
 380 time step as short as 0.0005 s to satisfy the stability criterion of the time marching step implemented in the  
 381 SPECFEM3D solver and accurate solutions of seismic waves up to the frequency of 10 Hz can be obtained. On  
 382 the other hand, the finiteness of the overall size of the considered spatial domain undermines the meaningfulness  
 383 of the modelling results for frequencies below 1 Hz. Each simulation consisted therefore in 16000 time  
 384 iterations with a computational cost amounting to approx. 900 CPU hours on 225 cores on the Galileo  
 385 supercomputer at CINECA.

387 **Results and discussion**

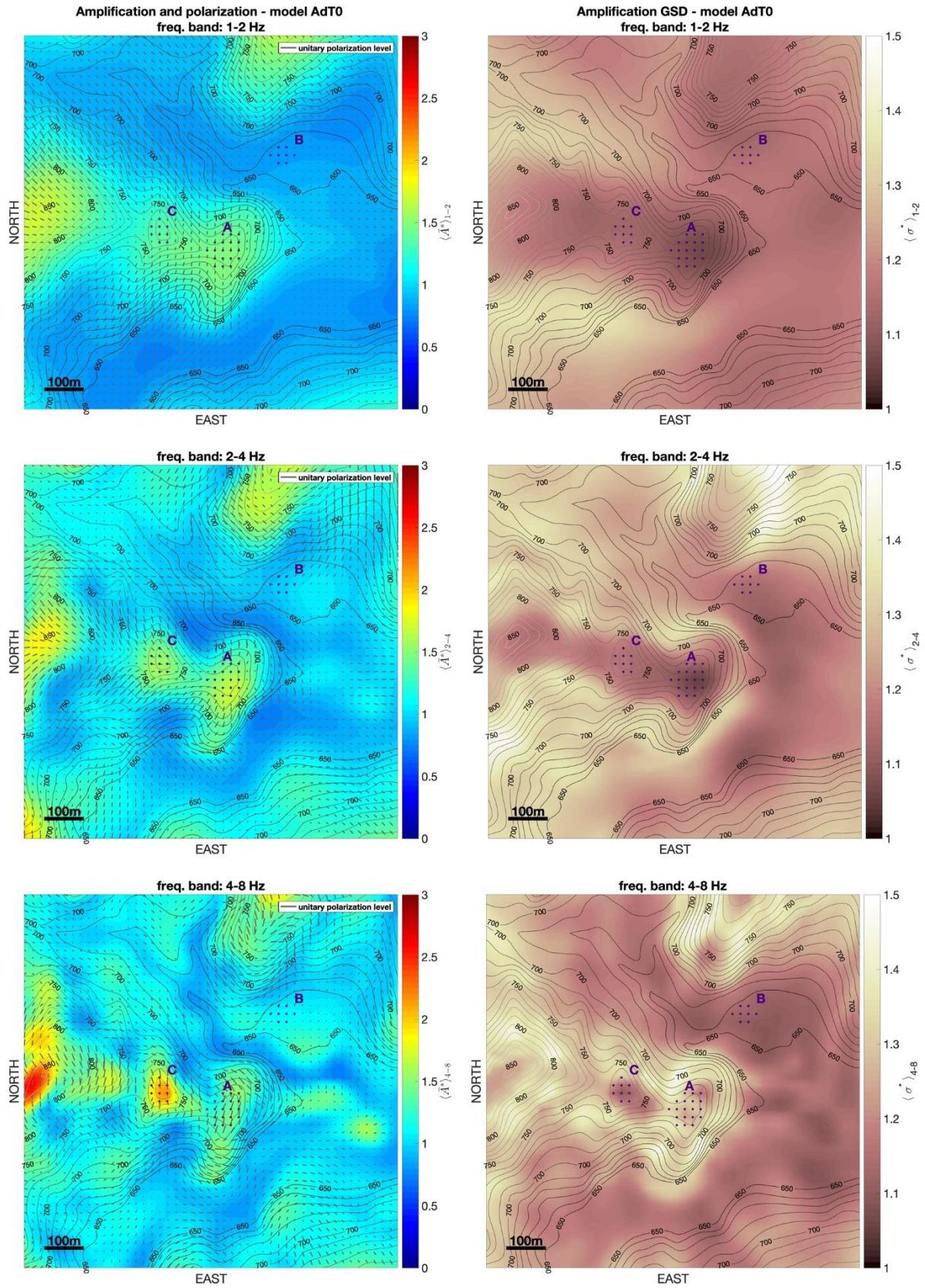
388 In order to identify the possible site effects that are due to surface morphology alone, we first computed the  
 389 numerical response functions (see eq. 3) for a homogeneous medium (model AdT0 in Table 1 and in Figure 3)  
 390 and evaluated over the topographic surface the geometric averages of the site response parameters defined in the  
 391 *Method* section. Successive computations regarding inhomogeneous media (models AdT1 and AdT2 in Table 1  
 392 and in Figure 3) allowed us to estimate the possible aggravations induced by the interaction between topography  
 393 and stratigraphy. In order to evaluate the meaningfulness of the aggravations in the spectral amplification due to  
 394 the changes in the model AdTx in respect to the reference model AdT0, (where AdTx stays for AdT1 or AdT2),  
 395 we estimated the *effect size*, defined as

$$396 \quad \Delta^{(AdTx)} = \frac{\bar{A}_{ln}^{(AdTx)} - \bar{A}_{ln}^{(AdT0)}}{\sigma_{ln}^{(AdT0)}}, \quad 17)$$

397 with  $\bar{A}_{ln}$  and  $\sigma_{ln}$  defined in equation (6). In consideration of the frequency dependence of the site response, we  
 398 summarize the results with maps representing the average value of the site response parameters functions over  
 399 defined frequency bands. In particular we considered the averages over the following frequency (period) bands:  
 400 1-2 Hz (0.5 -1 s), 2-4 Hz (0.25-0.5 s) and 4-8 Hz (0.125-0.25 s).

401 **Amplification**

402 In the homogenous medium hypothesis (model AdT0), the topographic features at Arquata del Tronto generate  
 403 amplification effects in all three considered frequency ranges, as can be observed from the maps exposed in  
 404 Figure 4. As expected, the amplification at a given frequency is controlled by topographic features with  
 405 characteristic sizes comparable with the associated wavelength (Geli et al. 1988). The average amplification  
 406 computed in the 1-2 Hz band correlates well with larger topographic features such as the whole Arquata hill,  
 407 while amplification in the 4-8 Hz band correlates well with smaller topographic features such as the top ridge of  
 408 Arquata and its N-S oriented secondary crests.



409  
410  
411

**Fig.4** left) distribution of horizontal plane-wave amplification and polarization computed for the homogeneous model in the three frequency bands 1-2Hz, 2-4Hz and 4-8Hz. Grey headless arrows in the maps in the left

412 column indicate the direction of polarization. The polarization level is indicated by the arrow length; right) the  
413 geometrical standard deviation corresponding to the amplification values on the left

414

415 Because of flat topography site B is unaffected by amplification in the considered bands, whereas sites A and C  
416 appear most affected in the 2-4 Hz and 4-8 Hz bands, respectively. The amplification however just exceeds the  
417 value 2 in the latter case. The geometric standard deviation is relatively low in the valley and along the top of  
418 the ridge in a strip whose width progressively decreases with frequency and almost vanishes in the high-  
419 frequency band.

420 The qualitative correspondence between topographic features and the response function amplitudes suggests that  
421 typical topographic effects could be speedily estimated from local morphometric variables. A promising  
422 approach in this sense is the Frequency-Scaled Curvature (FSC) introduced by Maufroy et al. (2015), who found  
423 a correlation between the seismic ground-motion amplification estimated with the median reference method  
424 MRM (Maufroy et al. 2012) and the general curvature  $\chi$  (defined in equation 16), with a wavelength-dependent  
425 smoothing applied on it. In analogy to Maufroy et al. (2015) we compared the plane wave amplification with the  
426 smoothed general curvature for different values of the smoothing length. We used the SAGA algorithm (Conrad  
427 et al. 2015) to evaluate the general curvature  $\chi$  at the surface points of the spatial domain and applied a  $n \times n$   
428 smoothing kernel, where  $n$  is an odd number which defines the smoothing length as  $L_s = 2 n D_x$  where  $D_x$  is the  
429 resolution of the DEM (10 m in our case).

430 Our comparison consists in the evaluation of the linear correlation coefficient  $r$  between the natural logarithm of  
431 the average value of the amplification function in the three frequency bands and the smoothed general curvature  
432  $\chi_{(L_s)}$ , where we express the smoothing length  $L_s$  in terms of the central wavelength  $\lambda_c$ , defined as the geometric  
433 mean of the wavelengths corresponding to the band extremes. From Fig. 5 it appears that the maximum  
434 correlation corresponds to a smoothing length  $L_s$  between  $0.5 \lambda_c$  and  $0.8 \lambda_c$ . This result is consistent with  
435 Maufroy et al. (2015), who established a maximum correlation between MRM amplification and smoothed  
436 curvature for a smoothing length of about half the wavelength. In the lower part of Fig. 5 we provide the  
437 weighted least squares linear regression between  $\langle \bar{A}_{ln} \rangle_{f_1-f_2}$  and  $\chi_{(L_s)}$  with  $L_s$  corresponding to the maximum  
438 correlation case. The coefficient of determination  $R^2$  reaches 0.8 in the 1-2 Hz frequency band but at higher  
439 frequencies the dispersion increases and  $R^2$  drops to 0.57 and 0.54 for the 2-4 Hz and 4-8 Hz band respectively.  
440 In Fig. 6 we can see how the horizontal amplification functions in the three sites A, B and C change because of  
441 the introduction of complexities in the model structure. The most remarkable changes concern site B, which is  
442 characterized by flat topography. The introduction of soil basin increases the amplification at site B to higher  
443 values than the topography-related amplification at sites A and C.

444 In the maps on the left side of Fig. 7 we represent the spatial distribution of  $\langle \bar{A}^* \rangle_{f_1-f_2}$  for the model AdT1, and  
445 on the right side the corresponding effect size in respect to the model AdT0.

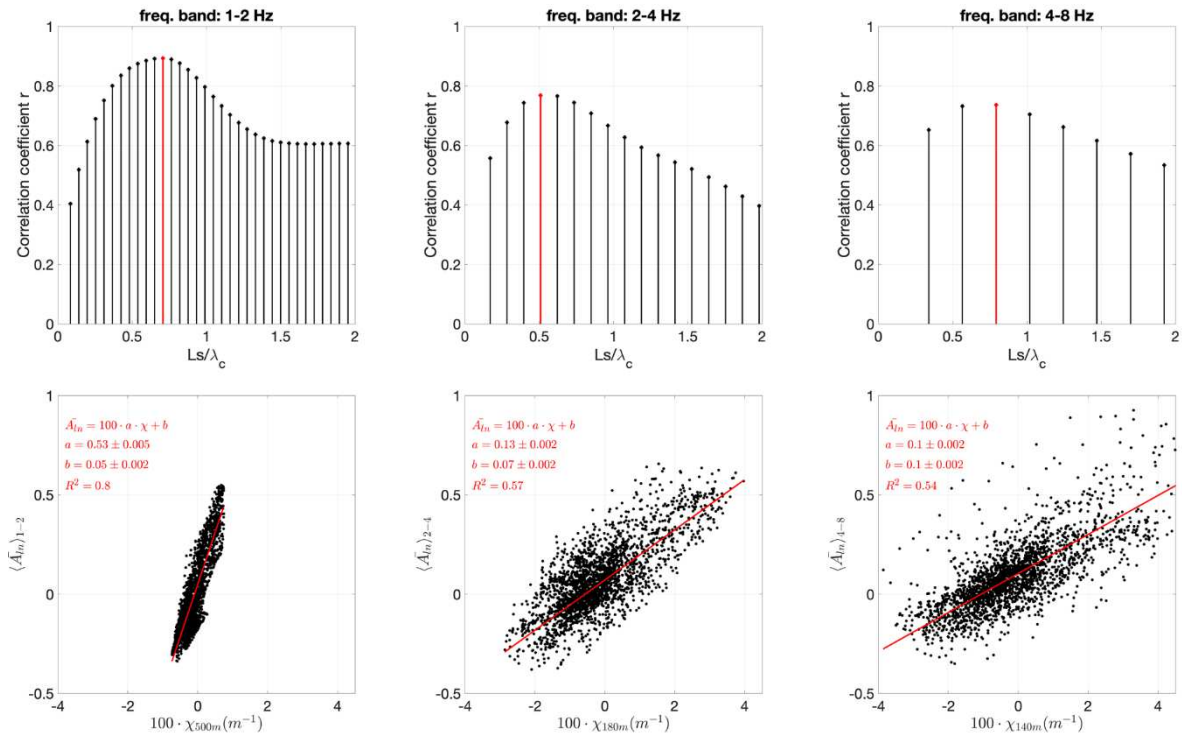
446 The AdT1 model differs from AdT0 in 25 m thick weathering layer just below the surface over all the area and a  
447 10 to 30 m thick layer of gravel deposits in the alluvial basin in the restricted area of Borgo (site B).

448 The weathering layer leads to a general increase of the amplification, with modulations that follow the  
449 topographic features. In the low frequency band ( $f < 2$  Hz) the increase in the amplification is not significant at  
450 any point, whereas in the intermediate and high frequency bands the amplification gain significance at some  
451 spots, but not on the flanks of the hills. The intermediate and high frequency amplification associated with the  
452 introduction of the soil layers in the alluvial basin at site B exceeds any amplification related to the interaction  
453 between topography and the weathering layer. The absence of amplification aggravation in the low frequency  
454 band can be easily explained if we consider that we assigned  $V_s=450$  m/s to the soil in the basin with a  
455 maximum depth of 30 m, which implies a stratigraphic amplification effects for frequencies above 3.75 Hz,  
456 whereas if we consider the combined effect of the basin and the weathering layer, the stratigraphic amplification  
457 does not affect frequencies below 2.5 Hz.

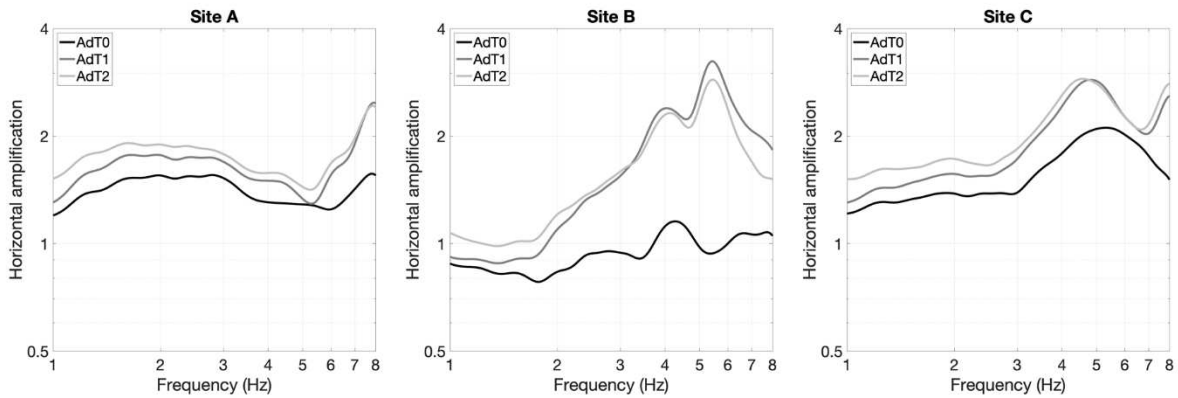
458 In Fig. 8 we represent an analogous comparison between the results concerning model AdT2 and model AdT0.  
459 The increase in the amplification that is due to the introduction of the deep structure (model AdT2) presents a  
460 pattern that is quite similar to the model AdT1, but with an overall effect size which is only slightly larger than  
461 in the AdT1 case.

462 In order to emphasize the differences in the effects of the models AdT2 and AdT1 compared to the model AdT0,  
463 we plot in Fig. 9 a histogram of the effect size values in the points on the map in the three considered frequency  
464 bands. The models AdT2 and AdT1 present differences in the amplification in the lowest frequency bands (1-2  
465 Hz and 2-4 Hz), whereas in the high frequency band (4-8 Hz) the two models are essentially equivalent. The  
466 broader distribution of the effect size values for the high frequency band in Fig. 9, can be explained with the  
467 sensitivity of the seismic response at high frequencies to small scale topographical and geological features.

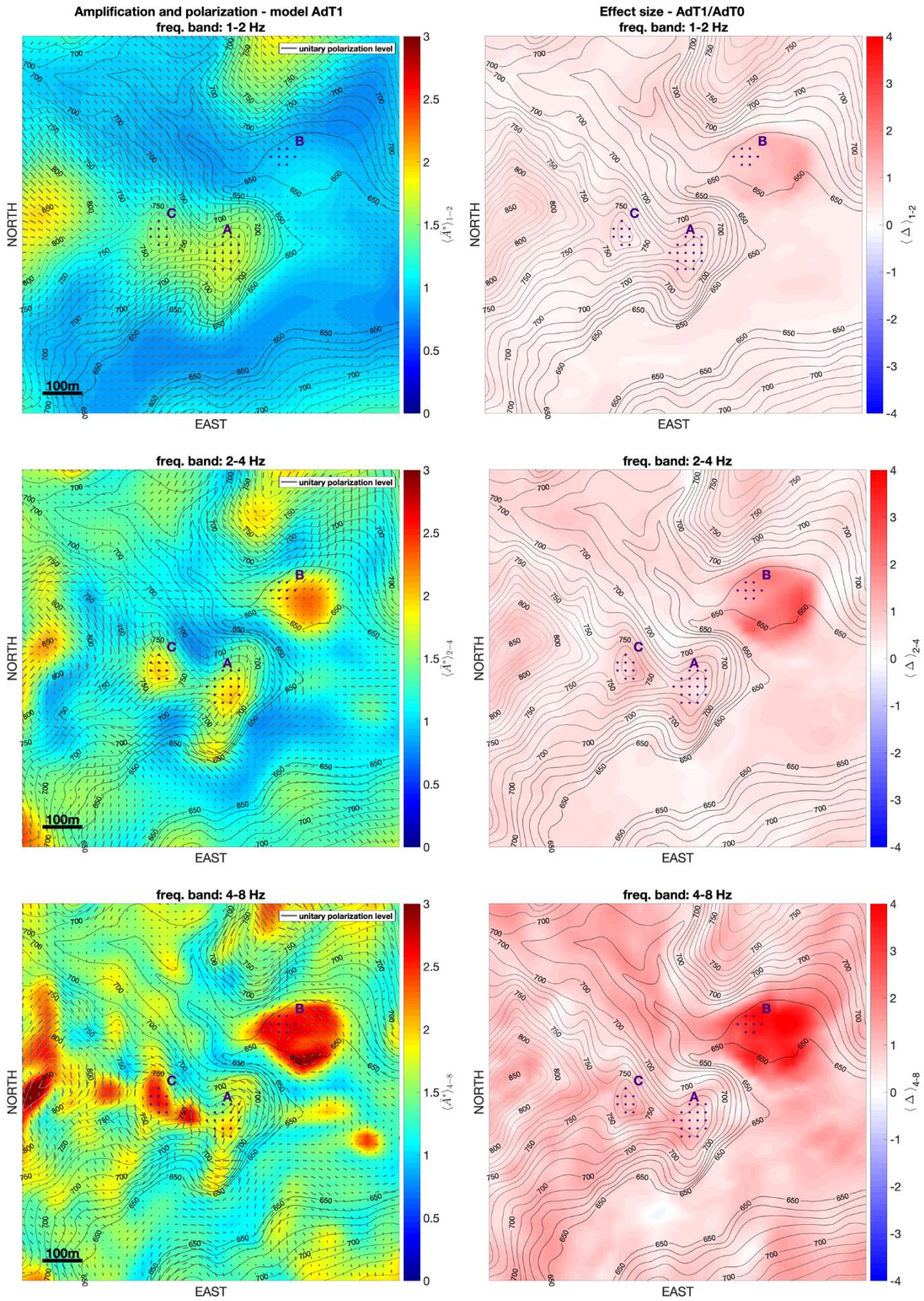
468  
469



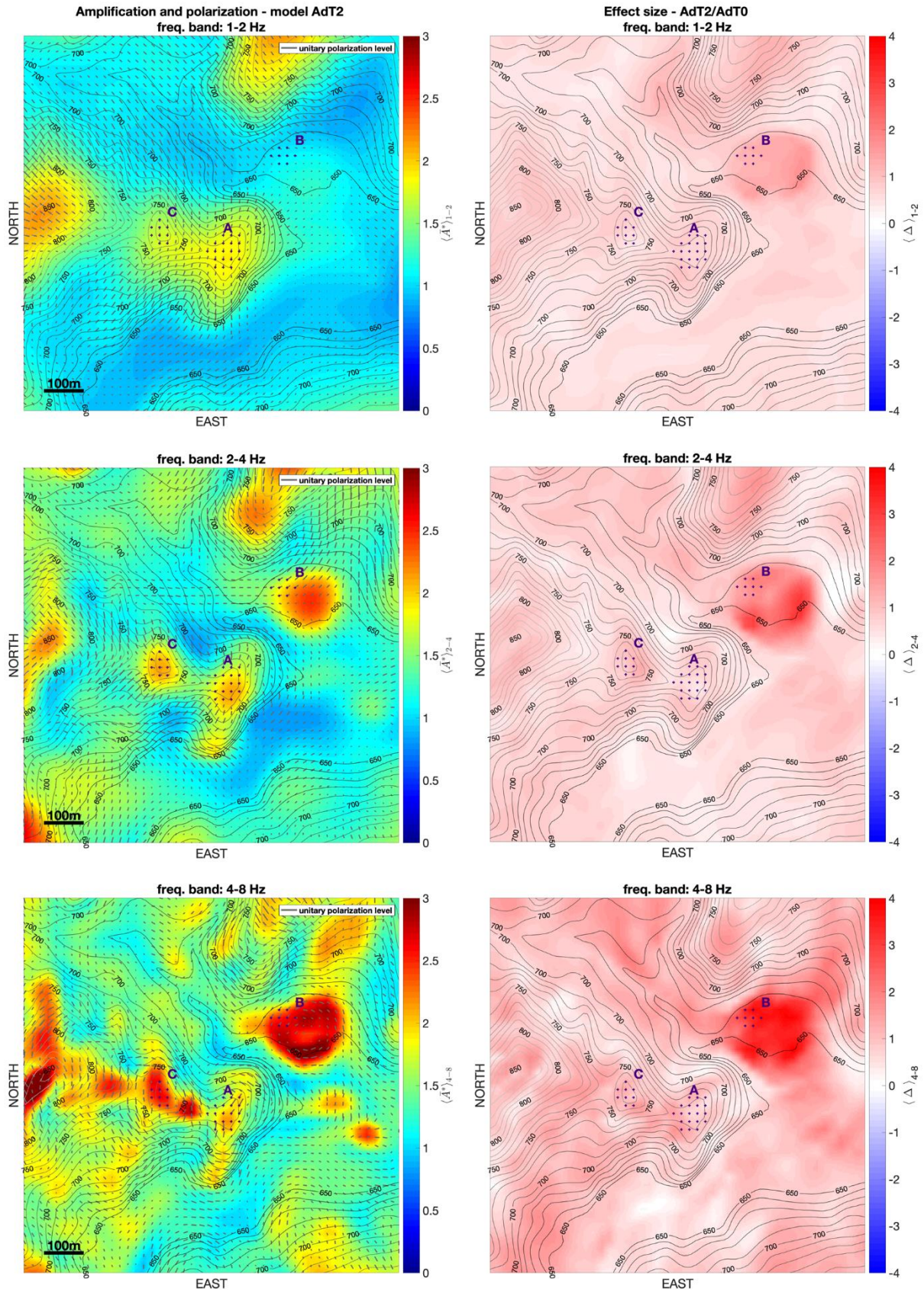
470  
471 **Fig.5** top) correlation coefficients between logarithmic plane-wave amplification  $\langle \bar{A}_{ln} \rangle_{f_1-f_2}$  and smoothed  
472 curvature  $\chi$  in three frequency bands for different values of the smoothing length  $Ls$ ; bottom) weighted-least  
473 square regression analysis between  $\langle \bar{A}_{ln} \rangle_{f_1-f_2}$  and smoothed  $\chi$  with smoothing length  $Ls$  corresponding to  
474 maximum correlation for each frequency band  
475



476  
477 **Fig.6** average horizontal plane-wave amplification at Site A (Arquata center), Site B (Borgo) and Site C  
478 (Arquata castle) for homogeneous AdT0 model (black), inhomogeneous AdT1 model (dark grey) and 3D model  
479 AdT2 (light grey). The average implies the stations covering each site, indicated as crossmarks in the maps in  
480 Fig.4  
481



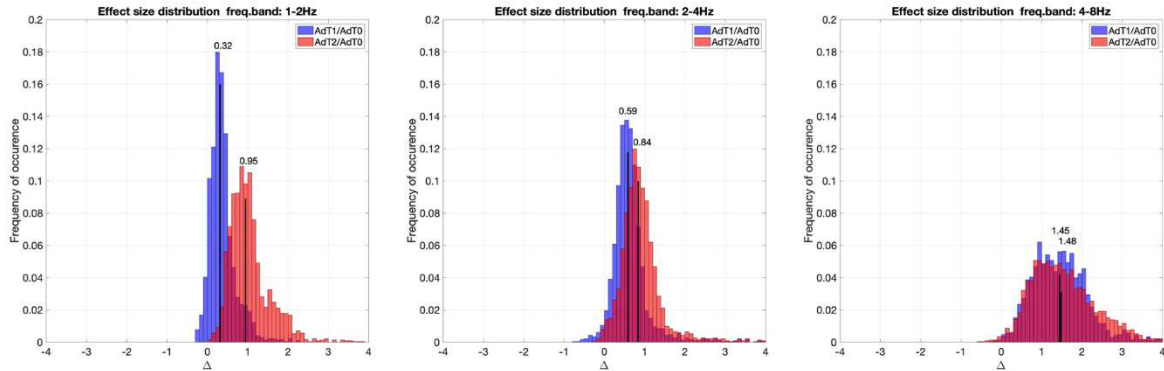
482  
 483 **Fig.7** left) horizontal plane-wave amplification distribution pattern at Arquata del Tronto computed for the  
 484 model AdT1 and in the frequency bands 1-2Hz, 2-4Hz and 4-8Hz. Same notation as in Fig.4; right) the effect  
 485 size (see Eq. 17 in the text) in the amplification values for the model AdT1 in respect to model AdT0



486  
487  
488  
489

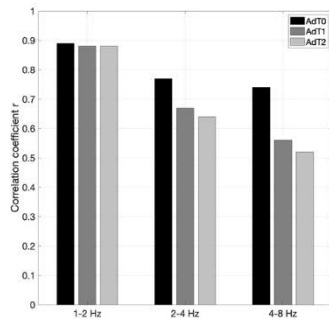
**Fig.8** left) horizontal plane-wave amplification distribution pattern at Arquata del Tronto computed for the model AdT2 and in the frequency bands 1-2Hz, 2-4Hz and 4-8Hz. Same notation as in Fig.4; right) the effect size (see Eq. 17 in the text) in the amplification values for the model AdT2 in respect to model AdT0

490  
491  
492



493  
494 **Fig.9** histograms of the amplification effect size values over the grid points sampling the studied area for the  
495 frequency bands: 1-2Hz, 2-4Hz and 4-8Hz. The median value is indicated in order to assess the overall  
496 differences between the changes in the amplification functions due to the variations in the structural models  
497

498 With the introduction of inhomogeneity in the model we found a frequency dependent drop in the correlation  
499 between the smoothed curvature and average amplification. In Figure 10 we plot the highest correlation scores  
500 for all the three investigated models in the three frequency bands. We note that in the 1-2 Hz band the  
501 heterogeneity in the model has almost no effect on the correlation between the amplification and the smoothed  
502 curvature. On the other hand, the variations in the subsurface model reduce substantially the correlation in the  
503 other two frequency bands, with the 4-8 Hz band being the most sensible to the subsurface structure effects, but  
504 without significant distinction between the two heterogeneous models.



505  
506 **Fig.10** correlation coefficients between averaged horizontal plane-wave amplification and smoothed curvature  
507 obtained in the three frequency bands of interest for homogeneous model AdT0 (black), inhomogeneous model  
508 AdT1 (dark grey) and 3D model AdT2 (light grey)  
509

### 510 Horizontal Polarization

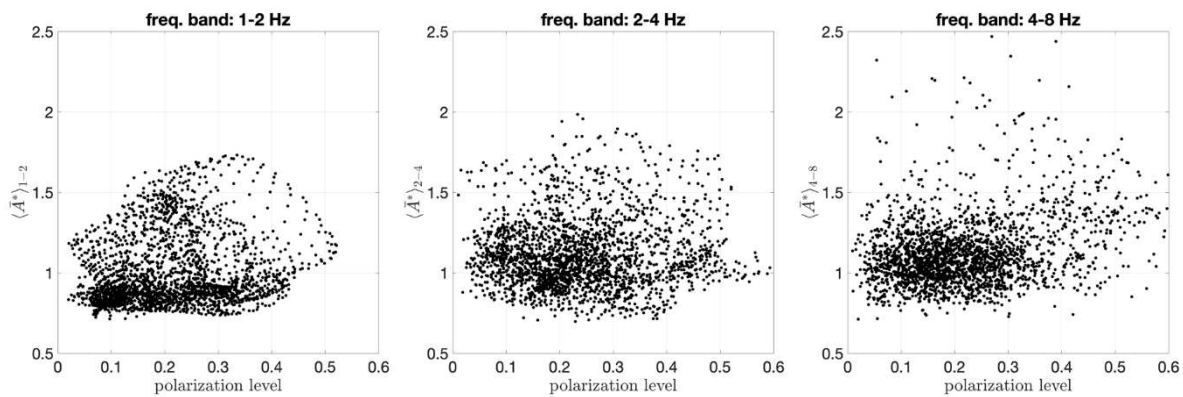
511 The distribution of the horizontal polarization in the site response for the model AdT0 is summarized on the  
512 maps on the left side in Fig.4, with the headless arrows indicating the direction  $\varphi_{max}$  of the maximum directional  
513 amplification averaged over the three frequency bands and the arrows' length indicating the polarization level  
514 defined as

$$515 \quad P = 1 - \frac{A_{\varphi_{min}}}{A_{\varphi_{max}}}, \quad (17)$$

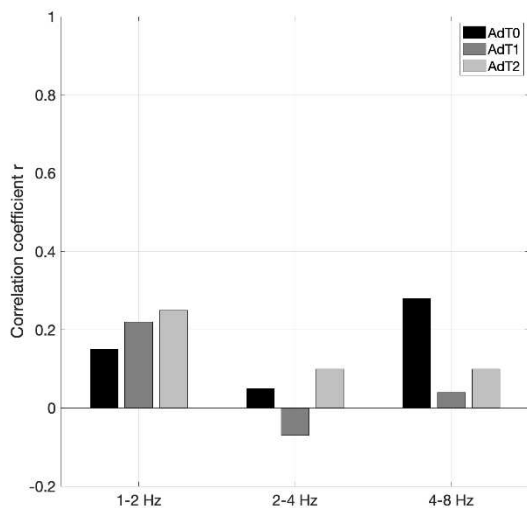
516 with  $A_{\varphi_{min}}$  and  $A_{\varphi_{max}}$  the minimum and the maximum directional amplifications at each point.  $P$  is zero when  
517 the amplification is isotropic and tends to 1 for increasing variability in the directional amplification.

518 We can observe that the direction and level of polarization change significantly in the three considered  
519 frequency bands. As can be seen from Fig.11 and Fig.12, the amplification appears to be generally uncorrelated  
520 with the polarization level: in many points the polarization of the response corresponds to directional de-  
521 amplification rather than amplification. This is the case of the polarization level found along the northern and

522 the southern slope of the Mt. Arquata ridge in the 1-2 Hz and 2-4 Hz bands. In the 2-4 Hz band the polarization  
523 level appears to be larger in the portion of the ridge's flanks that is closer to the top, but actually no clear  
524 relation between the polarization direction and the topographic features can be observed at these points, where  
525 polarization does not imply amplification. On the other hand, the points that are characterized by both  
526 polarization and amplification are essentially located on the primary and (in the 4-8 Hz band) secondary ridges.  
527 In this case the polarization direction is typically perpendicular to the crest orientation. We can therefore  
528 conclude that even if the topography-induced amplification is associated with polarization, the polarization itself  
529 does not necessarily implies topography-induced amplification.  
530 The introduction of the weathering layer and deeper structural units (Fig.7 and Fig.9, respectively), does not  
531 bring noticeable changes in the polarization pattern in the 1-2 Hz and 2-4 Hz bands, whereas in the 4-8 Hz band  
532 we can observe a reduction of the polarization level at site A on the edge of the ridge and the appearance of  
533 polarization in the seismic response at the edges of the nearly circular soil basin near site B, with direction  
534 tangential to the basin edge. The heterogeneous structure may therefore attenuate the topography-related  
535 polarization effects (without reducing the amplification) on one side and can produce topography-unrelated  
536 amplification and polarization, on the other.  
537



538  
539 **Fig.11** distribution of amplification values in function of the polarization level in the three frequency bands for  
540 the Model AdT0 case  
541



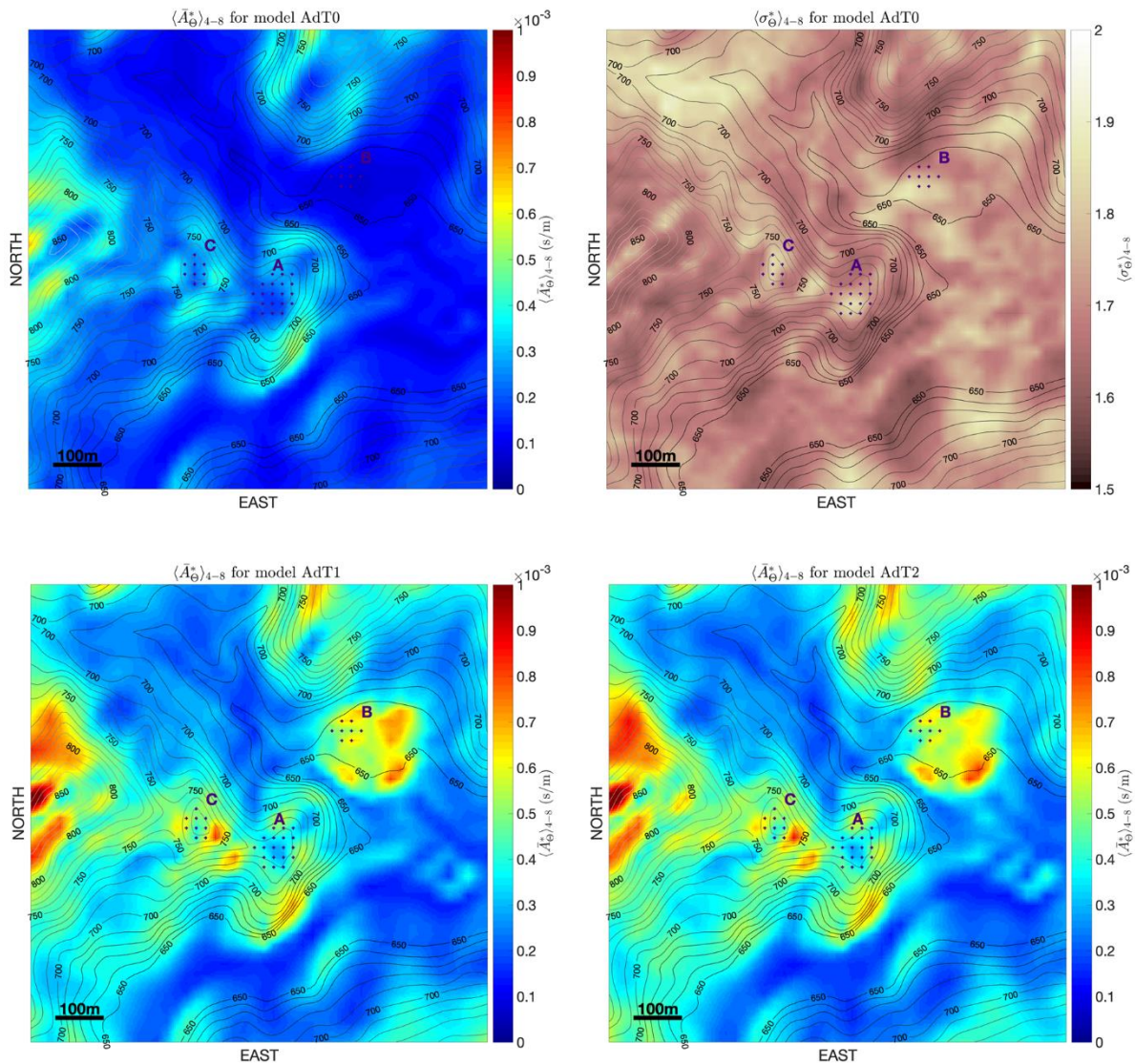
542  
543 **Fig.12** the values of the linear correlation coefficient between the polarization level and amplification  
544

### 545 Torsional motions

546 In Fig.13 we plot, for the three models, the maps corresponding to the average over the 4-8 Hz frequency band  
547 of the parameter  $\bar{A}_0^s$  defined in equation (14), which describes the scaling factor between the site-induced

548 angular velocity around the horizontal axis (i.e. torsional motion) and the translational acceleration of the  
 549 vertically incident plane wave. From the map corresponding to the homogeneous medium (model AdT0) it  
 550 appears that the highest values of the induced rotational motion are associated with the points on topographic  
 551 slopes, as predicted by the conceptual model that lead us to equation (13). The variability in  $\langle \bar{A}_\theta^* \rangle_{4-8\text{Hz}}$  is  
 552 described by a multiplicative standard deviation which ranges between a factor 1.5 and 2.  
 553 Maps regarding the frequency ranges 1-2 Hz and 2-4 Hz are available in the supplemental information as Figs.  
 554 S3 and S4.

555 From the maps regarding model AdT1 and model AdT2 in the frequency range 4-8 Hz (Fig.13), it is clear that  
 556 the introduction of the weathering layer enhances the rotational motion on the slopes whereas the introduction of  
 557 the basin structure produces rotations near the basin edges. These structure-induced rotations are of the same  
 558 order of magnitude of those induced by the concurrence of topography and weathering. We can also notice that  
 559 since they are characterized by low slope, the sites A and C are not affected by the appearance of torsional  
 560 components in the ground motion.  
 561



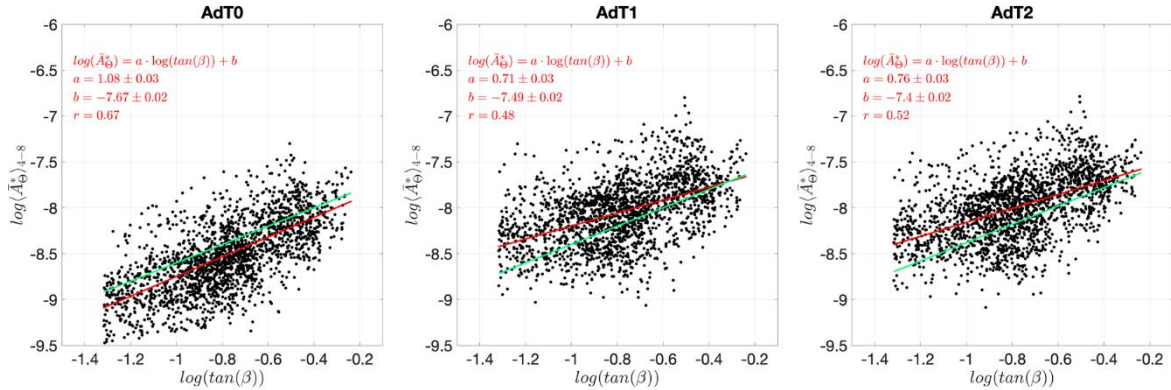
562  
 563 **Fig.13** scaling factor  $\bar{A}_\theta^*$  between the site-induced torsional motion and the translational acceleration of the  
 564 vertically incident plane wave, averaged in the frequency band 4-8Hz for the three models AdT0, AdT1 and  
 565 AdT2 and respective GSD  $\sigma_\theta^*$  for model AdT0  
 566

567 To verify quantitatively if equation (13) could be used to estimate the rotational scaling factor  $\langle \bar{A}_\theta^* \rangle_{4-8\text{Hz}}$   
 568 computed from the three models, we apply the weighted least squares approach to find the parameters a and b in  
 569 the linear fit

570  
571  
572  
573  
574  
575  
576  
577  
578

$$\langle \ln \bar{A}_\theta^* \rangle_{4-8\text{Hz}} = a \ln[\tan \beta] + b. \quad (16)$$

We consider the slope  $\beta$  distribution evaluated from the topography with the SAGA algorithm (Conrad et al. 2015), and apply a smoothing with length 125 m, corresponding to the wavelength of the incident waves at the maximum considered frequency (8 Hz). We neglect the points with slope  $\beta < 15^\circ$  in order to exclude from the analysis the rotation induced in the basin area near site B.



579  
580  
581  
582  
583  
584  
585  
586  
587  
588  
589

**Fig.14** weighted-least square regression (red line) between  $\langle \ln \bar{A}_\theta^* \rangle_{4-8\text{Hz}}$  and  $\ln[\tan(\beta)]$  at smoothing length  $L_s=125\text{m}$ , for the three models in the high frequency band (4-8 Hz). The green line indicates the expected regression (parameters  $a$  and  $b$  indicated in parenthesis in Tab.2)

The linear fit is shown in Fig. 14 and the parameters  $a$  and  $b$  corresponding to the three models are tabulated in Table 2 along with the  $V_s$  value interpreted from the  $b$  parameter. In parenthesis we give the target values consistent with equation (13).

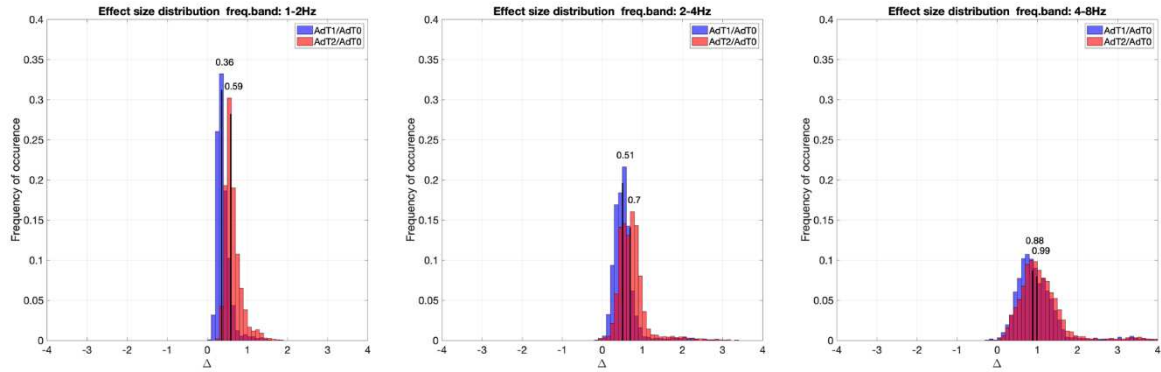
**Table 2** results of the weighted-least square analysis between  $\bar{A}_{\theta \ln}^*$  and  $\log(\tan(\beta))$  for the three models. Expected values for parameters  $a$  and  $b$  are given in parenthesis

	AdT0	AdT1	AdT2
$a$	1.08 (1.00)	0.71 (1.00)	0.76 (1.00)
$b$	-7.67 (-7.6)	-7.49 (-7.40)	-7.40 (-7.38)
$V_s=0.5 \exp(-b)$	1071 m/s (1000.0 m/s)	895 m/s (825 m/s)	818 m/s (806 m/s)

590  
591  
592  
593  
594  
595  
596  
597  
598  
599  
600  
601  
602  
603  
604  
605  
606  
607  
608

Regardless the relatively high dispersion of the  $\langle \ln \bar{A}_\theta^* \rangle_{4-8\text{Hz}}$  values (linear correlation  $r=0.67$ ), the AdT0 model provides a fit which is quite consistent with equation (13). As expected, the AdT1 and AdT2 models provides  $\langle \ln \bar{A}_\theta^* \rangle_{4-8\text{Hz}}$  values that are less correlated with the topographic slope. Even that the values of the parameter  $b$  for these two models are not too far from the ones corresponding to the harmonic mean of the  $V_s$  values in the weathering layer and in the underlying rock, the values of parameter  $a$  significantly deviate from unity, implying higher values of the scaling factor  $\bar{A}_\theta^*$  at moderate slope angles. In the cases where the topography effect combines with stratigraphic effects, we would need a more sophisticated predictive model than that provided in equation (13).

In figure 15 we analyze the differences between the effect size corresponding to the substitution of the AdT0 model with models AdT1 and AdT2, respectively. Only in the 4-8 Hz frequency band the median value of the effect size approaches unity, but in this frequency band the differences in the effect size of the two models are minimal. As in the amplification case, the 4-8 Hz band results the most sensible to the subsurface structure effects, without significant distinction between the two heterogeneous models. Even though the two heterogeneous models brings different levels of size effects in the other two frequency bands, these levels are below unity and could be considered less significant. The homogeneous model assumption is therefore sufficient to evaluate induced rotations in the frequency band up to 4 Hz.



609  
610  
611  
612  
613  
614  
615

**Fig.15** histograms of the induced torsional motion  $\bar{A}_0^*$  effect size values over the grid points sampling the studied area for the frequency bands: 1-2Hz, 2-4Hz and 4-8Hz. The median value is indicated in order to assess the overall differences between the changes in the amplification functions due to the variations in the structural models

## 616 Conclusions

617 In order to shed light on the three dimensional seismic local effects suffered by the Arquata del Tronto ridge  
618 under the 2016 Central Italy seismic sequence we set up a 3D numerical model of the area and computed the  
619 linear visco-elastic site response for a vertically incident plane wave by using the well-established software  
620 SPECFEM3D. In particular we analyzed the separated and combined effects of irregular topography and  
621 subsurface heterogeneity on the seismic ground motion in terms of horizontal component spectral amplification,  
622 including the aspects that concern polarization and rotation. To facilitate the discussion, we averaged the results  
623 over the frequency (period) bands of engineering interest: 1-2 Hz (0.5 -1 s or *low* frequency), 2-4 Hz (0.25-0.5 s  
624 or *intermediate* frequency) and 4-8 Hz (0.125-0.25 s or *high* frequency). By comparing the numerical results  
625 based on three different geophysical models of the area, one homogeneous, one with a weathering layer and one  
626 with a complex 3D structure, we were able to distinguish typical topographic effects from combined effects of  
627 topography and stratigraphy. We evaluated the intrinsic variability in the 3D seismic response caused by cross-  
628 coupling of different components of the ground motion by means of the sample standard deviation over a  
629 seismic input population composed of 200 three-component ground motion records collected in a station on  
630 seismic bedrock in the same geographical area. We used the evaluated standard deviation to estimate the effect  
631 size of the adoption of models with a heterogeneous structure instead of a homogeneous one.  
632 The obtained results permit to highlight the frequency dependence of topography-related amplification, which is  
633 controlled by topographic features with characteristic sizes comparable with the associated wavelength. For the  
634 homogeneous model, we found a good linear correlation between the plane wave amplification function and the  
635 topography's convexity, following the approach introduced by Maufroy et al. (2015). The maximum  
636 amplification values in a homogeneous model are however moderate (they do not exceed a factor of 2), but the  
637 introduction of the heterogeneous structure causes an aggravation, with modulations that follow the topographic  
638 and geological features. In the intermediate and high frequency bands, the aggravation is significant at some  
639 spots, in particular in the flat area occupied by the small alluvial basin, where the amplification equals and even  
640 exceeds the topography-related amplification at topographic highs. The correlation between amplification and  
641 curvature weakens for frequencies above 2 Hz, as soon as the weathering layer is considered in the structure,  
642 suggesting caution in the adoption of DEM-based proxies for site amplification in that frequency range.  
643 The directional analysis of the amplification in the homogeneous model show frequency dependence, as well. A  
644 visual analysis of the polarization level and angle distribution over the area, reveals that on the topographic  
645 reliefs, where the polarization is associated with convexity-related amplification, the polarization tends to be  
646 orthogonal to the topography major axis in the low frequency range, whereas in the high frequency range, the  
647 polarization changes and tends to be orthogonal to secondary ridges axes. The same analysis reveals that many  
648 points on the map are characterized by a polarized response that does not imply amplification. Actually we  
649 found that the polarization level is generally uncorrelated with the amplification. We conclude that even if the  
650 topography-induced amplification is associated with polarization, the polarization itself does not necessarily  
651 indicate amplification, since it could be associated with concavity-related de-amplification. A heterogeneous  
652 substratum seems to either attenuate the topography-related polarization effects or produce topography-  
653 unrelated amplification and polarization.

654 Finally, we analyzed the possibility of topography-induced torsional motions in terms of the scaling factor  
655 between the induced rotation rate and the seismic input acceleration. From simple geometrical considerations we  
656 expected a linear proportionality between the scaling factor and the tangent of the topographic slope, which was  
657 confirmed through a linear regression of the results concerning the homogeneous model case. On the other hand  
658 the introduction of the weathering layer clearly implies an aggravation of the induced torsional motion, especially  
659 in the high-frequency band. The torsional motion induced by the concurrence of slope and weathering appears to  
660 be of the same order of magnitude as that induced by the structural heterogeneity on the basin edge. This finding  
661 suggests that induced torsional motion could concur in the aggravation of earthquake effects on rocky hills like  
662 the one on which Arquata del Tronto rests.  
663 For both the translational and torsional components, the most evident aggravation of topography-related effects  
664 in respect to the homogeneous model is given by the introduction of the weathering layer in the frequency band  
665 4-8 Hz. On the other hand, the introduction of the 3D structure below the weathering layer implies a median  
666 aggravation that exceeds the one due to the introduction of the weathering layer in the band 1-4 Hz, but it  
667 appears relatively less significant if measured in respect to the variability of the 3D seismic response related to  
668 the components' cross-coupling.

669

## 670 **Declarations**

### 671 **Funding**

672 The research reported in this work was supported by OGS and CINECA under HPC-TRES program award  
673 number 2017-22 (J. B.).

674

### 675 **Conflicts of interest/Competing interests**

676 The authors declare no competing interests.

677

### 678 **Availability of data and material**

679 The topography data used in the present study is the 10 m resolution DEM Tinitaly available at  
680 <http://tinitaly.pi.ingv.it/>. Other material is available on request from the authors.

681

### 682 **Code availability**

683 The SPECSEM3D code is an open source software available on the Computational Infrastructure for  
684 Geodynamics (<http://geodynamics.org>). The 3D geological model was computed using the commercial software  
685 GeoModeller (<https://www.intrepid-geophysics.com/product/geomodeller>). Data processing and figures were  
686 done using MATLAB (<http://www.mathworks.com/products/matlab/>) and GMT ([https://www.generic-mapping-  
687 tools.org/](https://www.generic-mapping-tools.org/)).

688

### 689 **Authors' contributions**

690 All authors contributed to the study conception and design. Julie Baron performed the numerical simulations  
691 and data processing, Ilaria Primofiore edited the 3D geological models, Peter Klin provided the method  
692 description while Giovanna Vessia and Giovanna Laurenzano merged the parts and commented the results. All  
693 authors read and approved the final manuscript.

## 694 **References**

695 Amanti M, Muraro C, Roma M, et al (2020) Geological and geotechnical models definition for 3rd level seismic  
696 microzonation studies in Central Italy. Bull Earthq Eng 18:5441–5473. [https://doi.org/10.1007/s10518-  
697 020-00843-x](https://doi.org/10.1007/s10518-020-00843-x)

- 698 Anagnostopoulos SA, Kyrkos MT, Stathopoulos KG (2015) Earthquake induced torsion in buildings: critical  
699 review and state of the art. *Earthq Struct* 8:305–377. <https://doi.org/10.12989/eas.2015.8.2.305>
- 700 Ashford SA, Sitar N, Lysmer J, Deng N (1997) Topographic effects on the seismic response of steep slopes.  
701 *Bull Seismol Soc Am* 87:701–709
- 702 Assimaki D, Jeong S (2013) Ground-Motion Observations at Hotel Montana during the M 7.0 2010 Haiti  
703 Earthquake: Topography or Soil Amplification? *Bull Seismol Soc Am* 103:2577–2590.  
704 <https://doi.org/10.1785/0120120242>
- 705 Burjánek J, Edwards B, Fäh D (2014) Empirical evidence of local seismic effects at sites with pronounced  
706 topography: a systematic approach. *Geophys J Int* 197:608–619. <https://doi.org/10.1093/gji/ggu014>
- 707 Calcagno P, Chilès JP, Courrioux G, Guillen A (2008) Geological modelling from field data and geological  
708 knowledge: Part I. Modelling method coupling 3D potential-field interpolation and geological rules.  
709 *Phys Earth Planet Inter* 171:147–157. <https://doi.org/10.1016/j.pepi.2008.06.013>
- 710 Castellani A, Stupazzini M, Guidotti R (2012) Free-field rotations during earthquakes: Relevance on buildings.  
711 *Earthq Eng Struct Dyn* 41:875–891. <https://doi.org/10.1002/eqe.1163>
- 712 Conrad O, Bechtel B, Bock M, et al (2015) System for Automated Geoscientific Analyses (SAGA) v. 2.1.4.  
713 *Geosci Model Dev* 8:1991–2007. <https://doi.org/10.5194/gmd-8-1991-2015>
- 714 Cruz-Atienza VM, Tago J, Sanabria-Gómez JD, et al (2016) Long Duration of Ground Motion in the  
715 Paradigmatic Valley of Mexico. *Sci Rep* 6:38807. <https://doi.org/10.1038/srep38807>
- 716 Evans JR, International Working Group on Rotational Seismology (2009) Suggested Notation Conventions for  
717 Rotational Seismology. *Bull Seismol Soc Am* 99:1073–1075. <https://doi.org/10.1785/0120080060>
- 718 Fehr M, Kremers S, Fritschen R (2019) Characterisation of seismic site effects influenced by near-surface  
719 structures using 3D waveform modelling. *J Seismol* 23:373–392. <https://doi.org/10.1007/s10950-018-09811-0>
- 720
- 721 Galli P, Peronace E, Tertulliani A (2016) Rapporto sugli effetti macrosismici del terremoto del 24 Agosto 2016  
722 di Amatrice in scala MCS. Zenodo
- 723 Geli L, Bard P-Y, Jullien B (1988) The effect of topography on earthquake ground motion: A review and new  
724 results. *Bull Seismol Soc Am* 78:42–63
- 725 Giallini S, Pizzi A, Pagliaroli A, et al (2020) Evaluation of complex site effects through experimental methods  
726 and numerical modelling: The case history of Arquata del Tronto, central Italy. *Eng Geol* 272:105646.  
727 <https://doi.org/10.1016/j.enggeo.2020.105646>
- 728 Graizer V (2009) Low-velocity zone and topography as a source of site amplification effect on Tarzana hill,  
729 California. *Soil Dyn Earthq Eng* 29:324–332. <https://doi.org/10.1016/j.soildyn.2008.03.005>
- 730 Grelle G, Wood C, Bonito L, et al (2018) A reliable computerized litho-morphometric model for development  
731 of 3D maps of Topographic Aggravation Factor (TAF): the cases of East Mountain (Utah, USA) and  
732 Port au Prince (Haiti). *Bull Earthq Eng* 16:1725–1750. <https://doi.org/10.1007/s10518-017-0272-x>
- 733 Guidotti R, Castellani A, Stupazzini M (2018) Near-Field Earthquake Strong Ground Motion Rotations and  
734 Their Relevance on Tall Buildings. *Bull Seismol Soc Am* 108:1171–1184.  
735 <https://doi.org/10.1785/0120170140>
- 736 Hailemikael S, Lenti L, Martino S, et al (2016) Ground-motion amplification at the Colle di Roio ridge, central  
737 Italy: a combined effect of stratigraphy and topography. *Geophys J Int* 206:1–18.  
738 <https://doi.org/10.1093/gji/ggw120>

- 739 ISPRA (2018) Relazione Illustrativa dello Studio di Microzonazione Sismica propedeutico al Livello 3 della  
740 Macroarea 1 Arquata del Tronto e Montegalfo (AP) e Allegati (in italian). Rome
- 741 Klin P, Laurenzano G, Romano MA, et al (2019) ER3D: a structural and geophysical 3-D model of central  
742 Emilia-Romagna (northern Italy) for numerical simulation of earthquake ground motion. *Solid Earth*  
743 10:931–949. <https://doi.org/10.5194/se-10-931-2019>
- 744 Lanzo G, Tommasi P, Ausilio E, et al (2019) Reconnaissance of geotechnical aspects of the 2016 Central Italy  
745 earthquakes. *Bull Earthq Eng* 17:5495–5532. <https://doi.org/10.1007/s10518-018-0350-8>
- 746 Laurenzano G, Barnaba C, Romano MA, et al (2019) The Central Italy 2016–2017 seismic sequence: site  
747 response analysis based on seismological data in the Arquata del Tronto–Montegalfo municipalities.  
748 *Bull Earthq Eng* 17:5449–5469. <https://doi.org/10.1007/s10518-018-0355-3>
- 749 Lee VW, Trifunac MD (1985) Torsional accelerograms. *Int J Soil Dyn Earthq Eng* 4:132–139.  
750 [https://doi.org/10.1016/0261-7277\(85\)90007-5](https://doi.org/10.1016/0261-7277(85)90007-5)
- 751 Lee WHK, Çelebi M, Todorovska MI, Igel H (2009) Introduction to the Special Issue on Rotational Seismology  
752 and Engineering Applications. *Bull Seismol Soc Am* 99:945–957. <https://doi.org/10.1785/0120080344>
- 753 Luo Y, Fan X, Huang R, et al (2020) Topographic and near-surface stratigraphic amplification of the seismic  
754 response of a mountain slope revealed by field monitoring and numerical simulations. *Eng Geol*  
755 271:105607. <https://doi.org/10.1016/j.enggeo.2020.105607>
- 756 Massa M, Barani S, Lovati S (2014) Overview of topographic effects based on experimental observations:  
757 meaning, causes and possible interpretations. *Geophys J Int* 197:1537–1550.  
758 <https://doi.org/10.1093/gji/ggt341>
- 759 Maufroy E, Cruz-Atienza VM, Cotton F, Gaffet S (2015) Frequency-Scaled Curvature as a Proxy for  
760 Topographic Site-Effect Amplification and Ground-Motion Variability. *Bull Seismol Soc Am*  
761 105:354–367. <https://doi.org/10.1785/0120140089>
- 762 Maufroy E, Cruz-Atienza VM, Gaffet S (2012) A Robust Method for Assessing 3-D Topographic Site Effects:  
763 A Case Study at the LSBB Underground Laboratory, France. *Earthq Spectra* 28:1097–1115.  
764 <https://doi.org/10.1193/1.4000050>
- 765 Moore ID, Grayson RB, Ladson AR (1991) Digital terrain modelling: A review of hydrological,  
766 geomorphological, and biological applications. *Hydrol Process* 5:3–30.  
767 <https://doi.org/10.1002/hyp.3360050103>
- 768 Newmark N (1969) Torsion in symmetrical buildings. In: *Proceedings of the 4th World Conference Earthq.*  
769 *Eng. ASCE*
- 770 Paolucci R (2002) Amplification of earthquake ground motion by steep topographic irregularities. *Earthq Eng*  
771 *Struct Dyn* 31:1831–1853. <https://doi.org/10.1002/eqe.192>
- 772 Paolucci R (1999) Numerical evaluation of the effect of cross-coupling of different components of ground  
773 motion in site response analyses. *Bull Seismol Soc Am* 89:877–887
- 774 Paolucci R, Mazzieri I, Smerzini C (2015) Anatomy of strong ground motion: near-source records and three-  
775 dimensional physics-based numerical simulations of the Mw 6.0 2012 May 29 Po Plain earthquake,  
776 Italy. *Geophys J Int* 203:2001–2020. <https://doi.org/10.1093/gji/ggv405>
- 777 Pedersen H, Le Brun B, Hatzfeld D, et al (1994) Ground-motion amplitude across ridges. *Bull Seismol Soc Am*  
778 84:1786–1800
- 779 Peter D, Komatitsch D, Luo Y, et al (2011) Forward and adjoint simulations of seismic wave propagation on  
780 fully unstructured hexahedral meshes. *Geophys J Int* 186:721–739. <https://doi.org/10.1111/j.1365-246X.2011.05044.x>  
781

- 782 Pischiutta M, Cianfarra P, Salvini F, et al (2018) A systematic analysis of directional site effects at stations of  
783 the Italian seismic network to test the role of local topography. *Geophys J Int* 214:635–650.  
784 <https://doi.org/10.1093/gji/ggy133>
- 785 Primofiore I, Baron J, Klin P, et al (2020) 3D numerical modelling for interpreting topographic effects in rocky  
786 hills for Seismic Microzonation: The case study of Arquata del Tronto hamlet. *Eng Geol* 279:105868.  
787 <https://doi.org/10.1016/j.enggeo.2020.105868>
- 788 Puglia R, Vona M, Klin P, et al (2013) Analysis of Site Response and Building Damage Distribution Induced by  
789 the 31 October 2002 Earthquake at San Giuliano di Puglia (Italy). *Earthq Spectra* 29:497–526.  
790 <https://doi.org/10.1193/1.4000134>
- 791 Puzzilli LM, Ferri F, Eulilli V, et al (2019) Integrated geophysical methods for the seismic site characterization  
792 of Arquata del Tronto. Roma, Italy
- 793 Savage B, Komatitsch D, Tromp J (2010) Effects of 3D Attenuation on Seismic Wave Amplitude and Phase  
794 Measurements. *Bull Seismol Soc Am* 100:1241–1251. <https://doi.org/10.1785/0120090263>
- 795 Seriani G, Priolo E (1994) Spectral element method for acoustic wave simulation in heterogeneous media. *Finite*  
796 *Elem Anal Des* 16:337–348. [https://doi.org/10.1016/0168-874X\(94\)90076-0](https://doi.org/10.1016/0168-874X(94)90076-0)
- 797 Spudich P, Fletcher JB (2008) Observation and Prediction of Dynamic Ground Strains, Tilts, and Torsions  
798 Caused by the Mw 6.0 2004 Parkfield, California, Earthquake and Aftershocks, Derived from UPSAR  
799 Array Observations. *Bull Seismol Soc Am* 98:1898–1914. <https://doi.org/10.1785/0120070157>
- 800 Stupazzini M, de la Puente J, Smerzini C, et al (2009) Study of Rotational Ground Motion in the Near-Field  
801 Region. *Bull Seismol Soc Am* 99:1271–1286. <https://doi.org/10.1785/0120080153>
- 802 Tarquini S, Isola I, Favalli M, et al (2007) TINITALY/01: a new Triangular Irregular Network of Italy. *Ann*  
803 *Geophys* 50:407–425. <https://doi.org/10.4401/ag-4424>
- 804 Wood CM, Cox BR (2016) Comparison of Field Data Processing Methods for the Evaluation of Topographic  
805 Effects. *Earthq Spectra* 32:2127–2147. <https://doi.org/10.1193/111515EQS170M>
- 806 Xie Z, Komatitsch D, Martin R, Matzen R (2014) Improved forward wave propagation and adjoint-based  
807 sensitivity kernel calculations using a numerically stable finite-element PML. *Geophys J Int* 198:1714–  
808 1747. <https://doi.org/10.1093/gji/ggu219>
- 809 Zevenbergen LW, Thorne CR (1987) Quantitative analysis of land surface topography. *Earth Surf Process*  
810 *Landf* 12:47–56. <https://doi.org/10.1002/esp.3290120107>
- 811 Zhou H, Li J, Chen X (2020) Establishment of a seismic topographic effect prediction model in the Lushan Ms  
812 7.0 earthquake area. *Geophys J Int* 221:273–288. <https://doi.org/10.1093/gji/ggaa003>
- 813

# Figures

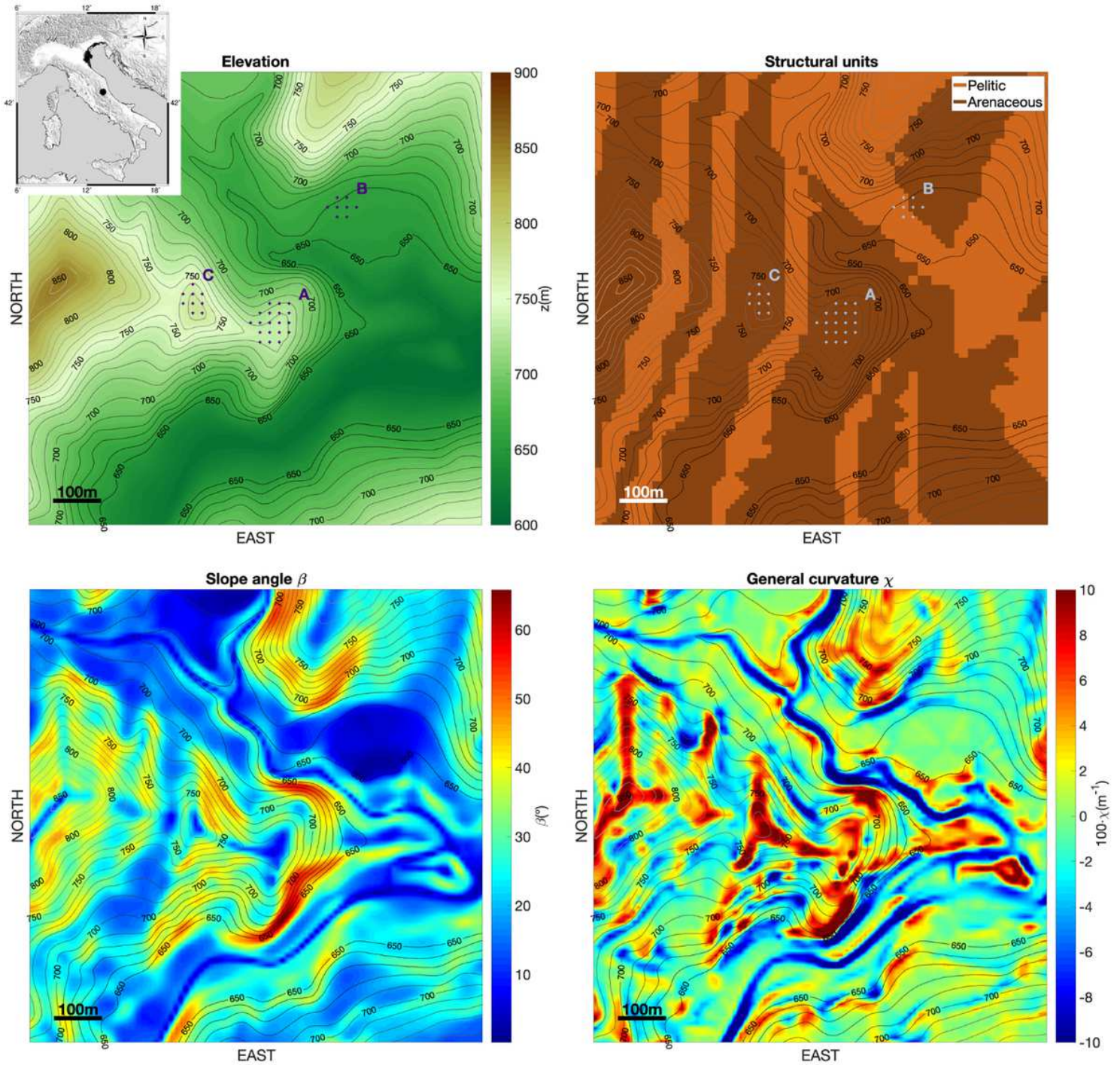
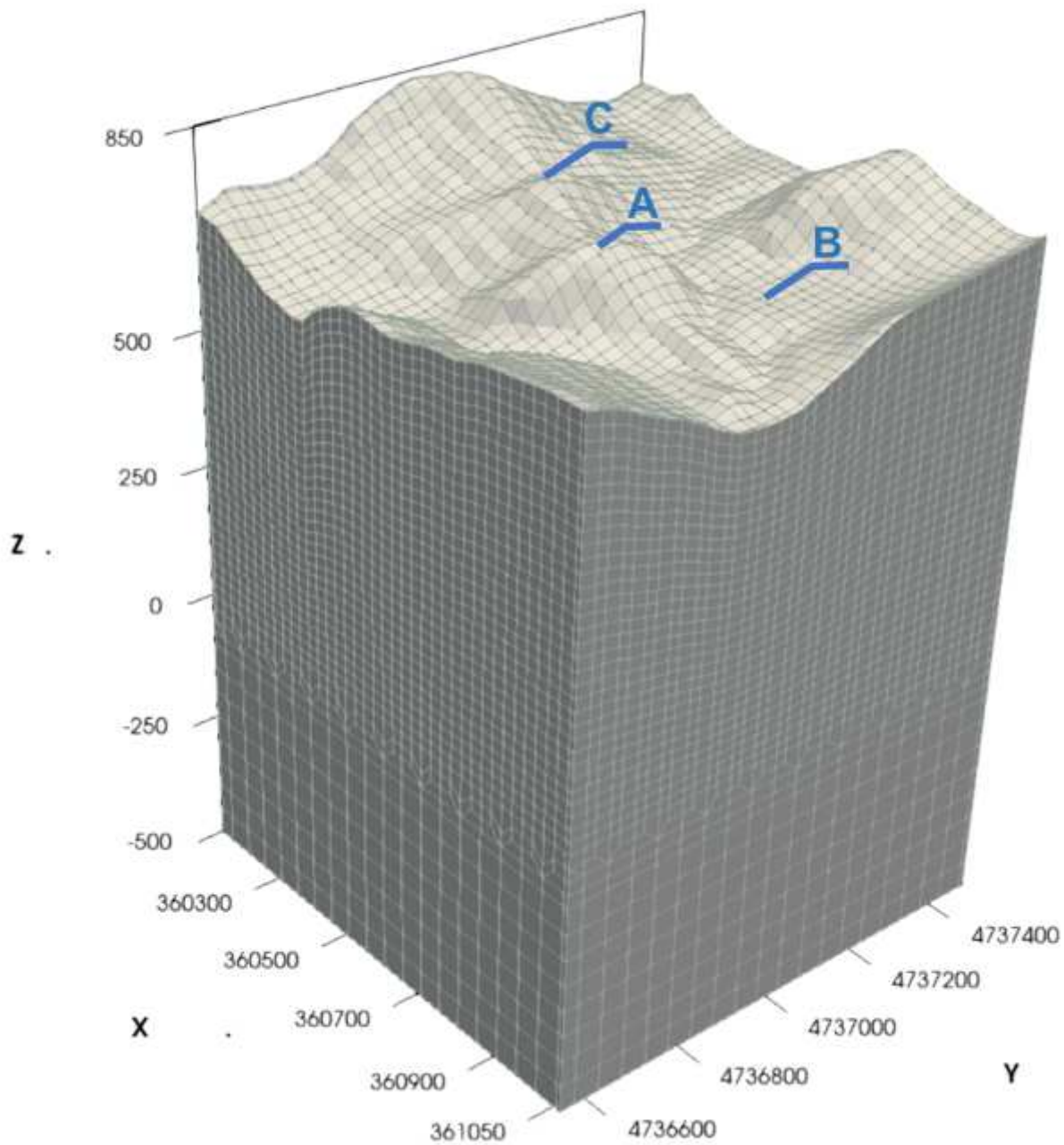


Figure 1

topographic and morphologic characterization of the studied area. The location of the area in the Italian peninsula is evidenced with the black dot in the small map overlapping the elevation map (upper left). The cross marks in the elevation map indicate the virtual seismic stations in three sites of interest: site A corresponds to Arquata del Tronto hamlet, site B to Borgo in the valley and Site C to the Castle promontory. In the structural model map (upper right) we depict the alternance of pelitic and arenaceous

formations just below the weathering layer. The topographic slope and curvature are shown in the bottom left and right maps respectively



**Figure 2**

the central portion of the numerical mesh used for numerical simulations. The locations of the sites A, B and C are shown. Length units are in meters, x-direction is eastward

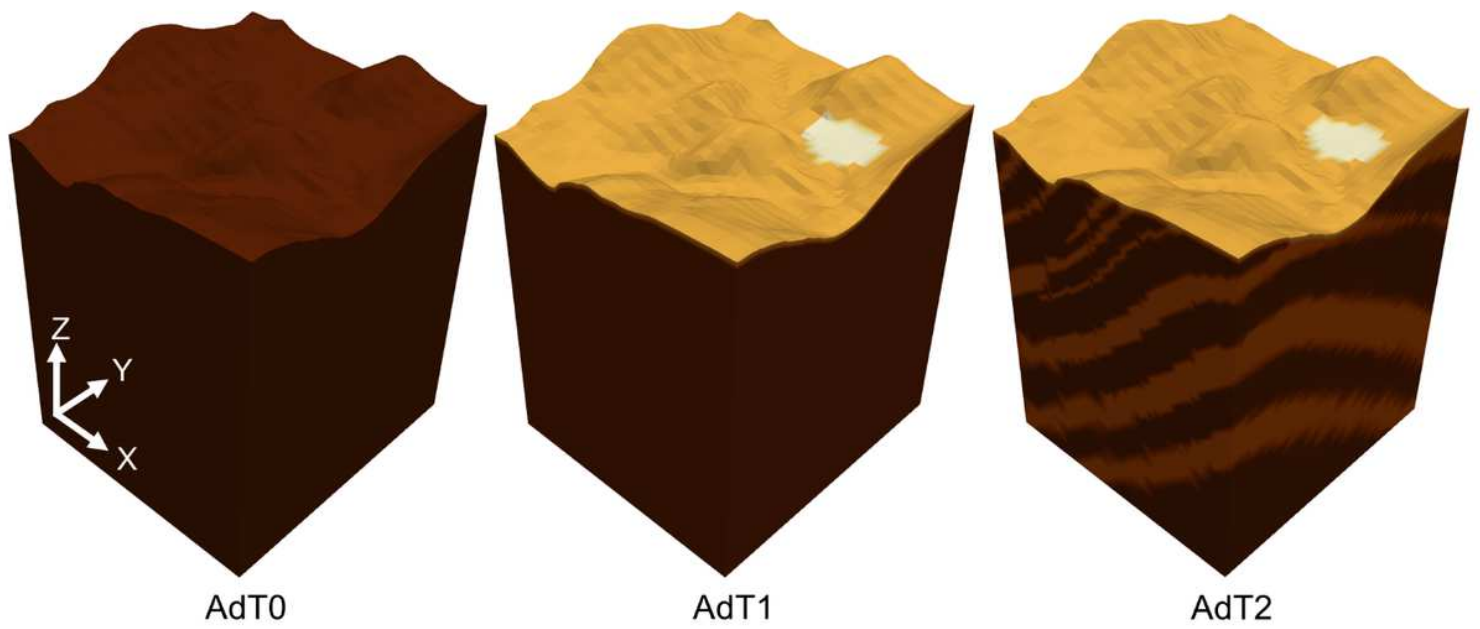


**Figure 3**

representation of the three input models clipped on the 1 km<sup>2</sup> square area of interest. AdT0 is the homogeneous model, AdT1 is the homogeneous model with a weathering layer and an alluvial, AdT2 is the full 3D model of Arquata del Tronto retrieved from Primofiore et al. (2020)

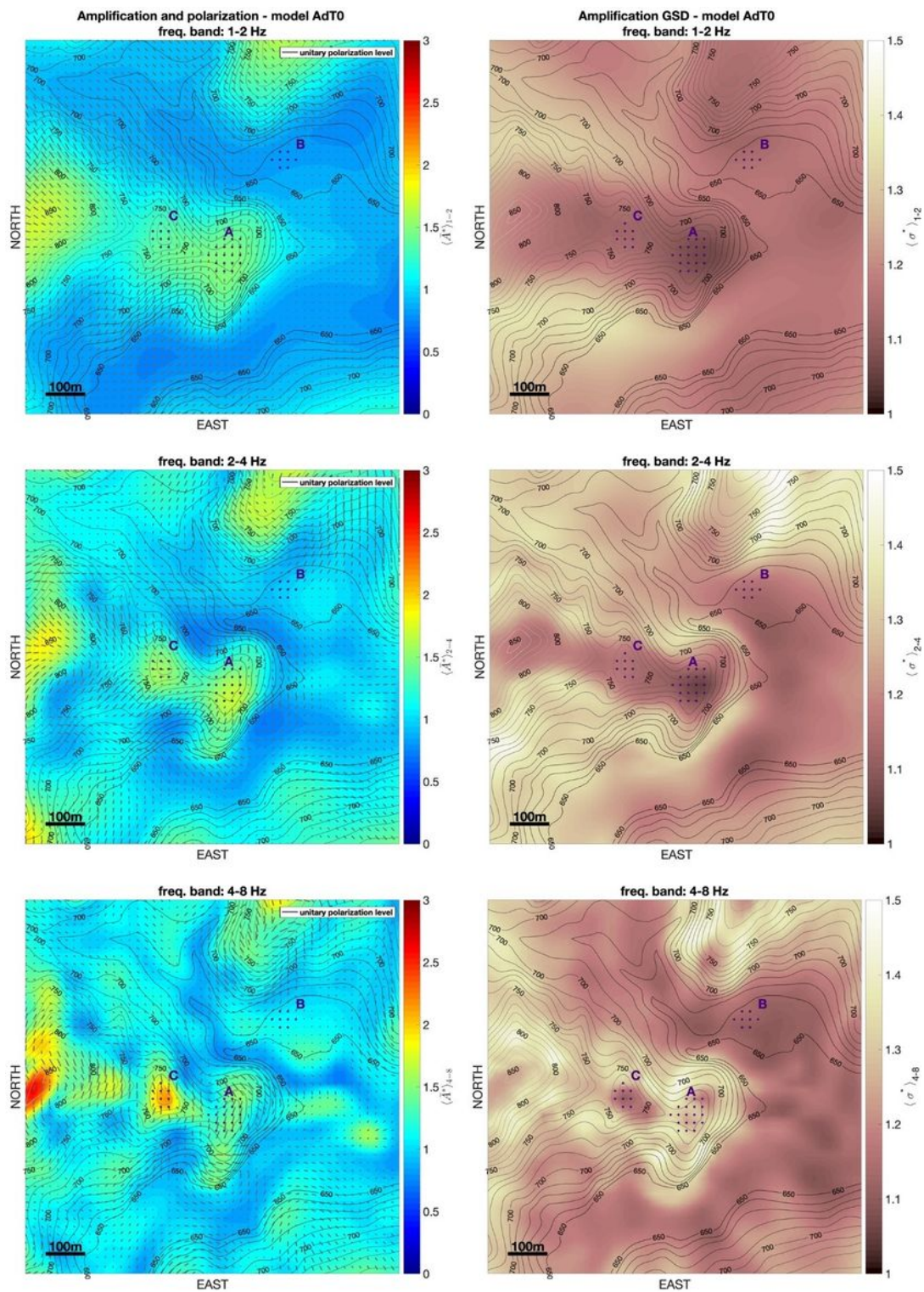


**Figure 4**

left) distribution of horizontal plane-wave amplification and polarization computed for the homogeneous model in the three frequency bands 1-2Hz, 2-4Hz and 4-8Hz. Grey headless arrows in the maps in the left column indicate the direction of polarization. The polarization level is indicated by the arrow length; right) the geometrical standard deviation corresponding to the amplification values on the left

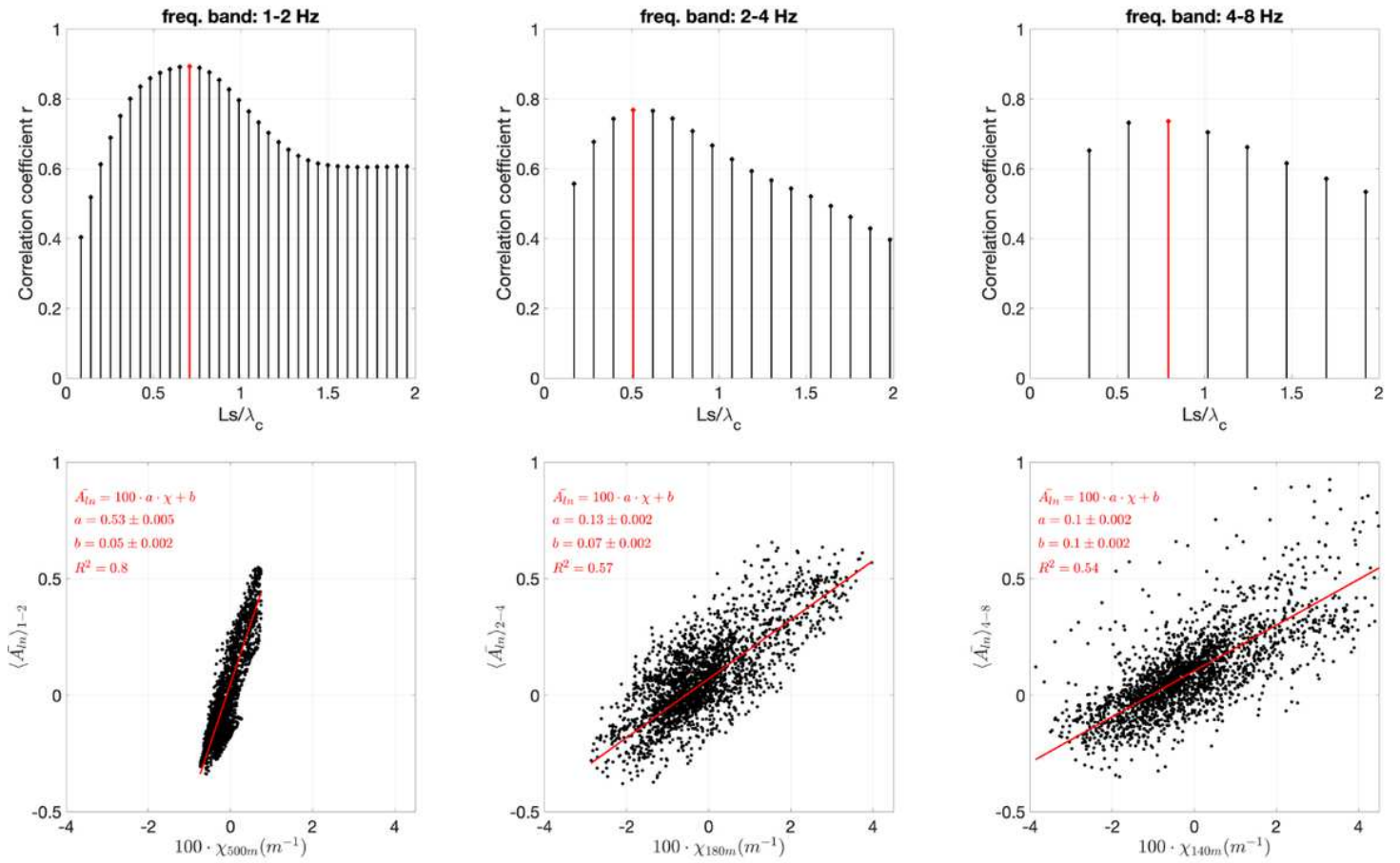


Figure 5

Please see the Manuscript PDF file for the complete figure caption.

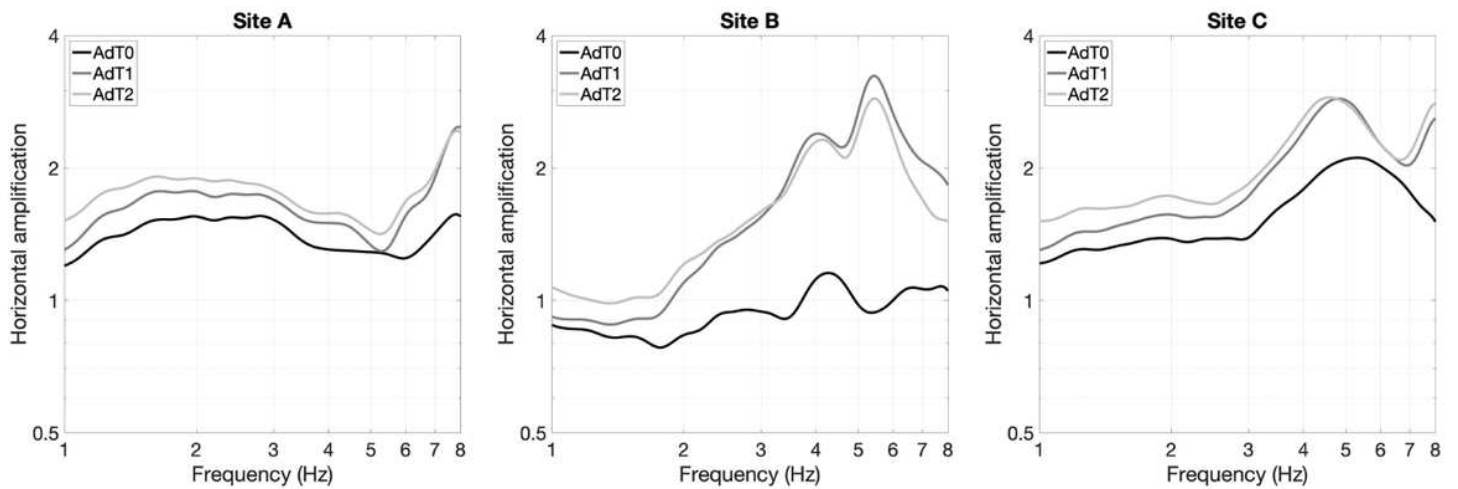


Figure 6

average horizontal plane-wave amplification at Site A (Arquata center), Site B (Borgo) and Site C (Arquata castle) for homogeneous AdT0 model (black), inhomogeneous AdT1 model (dark grey) and 3D model

AdT2 (light grey). The average implies the stations covering each site, indicated as crossmarks in the maps in Fig.4

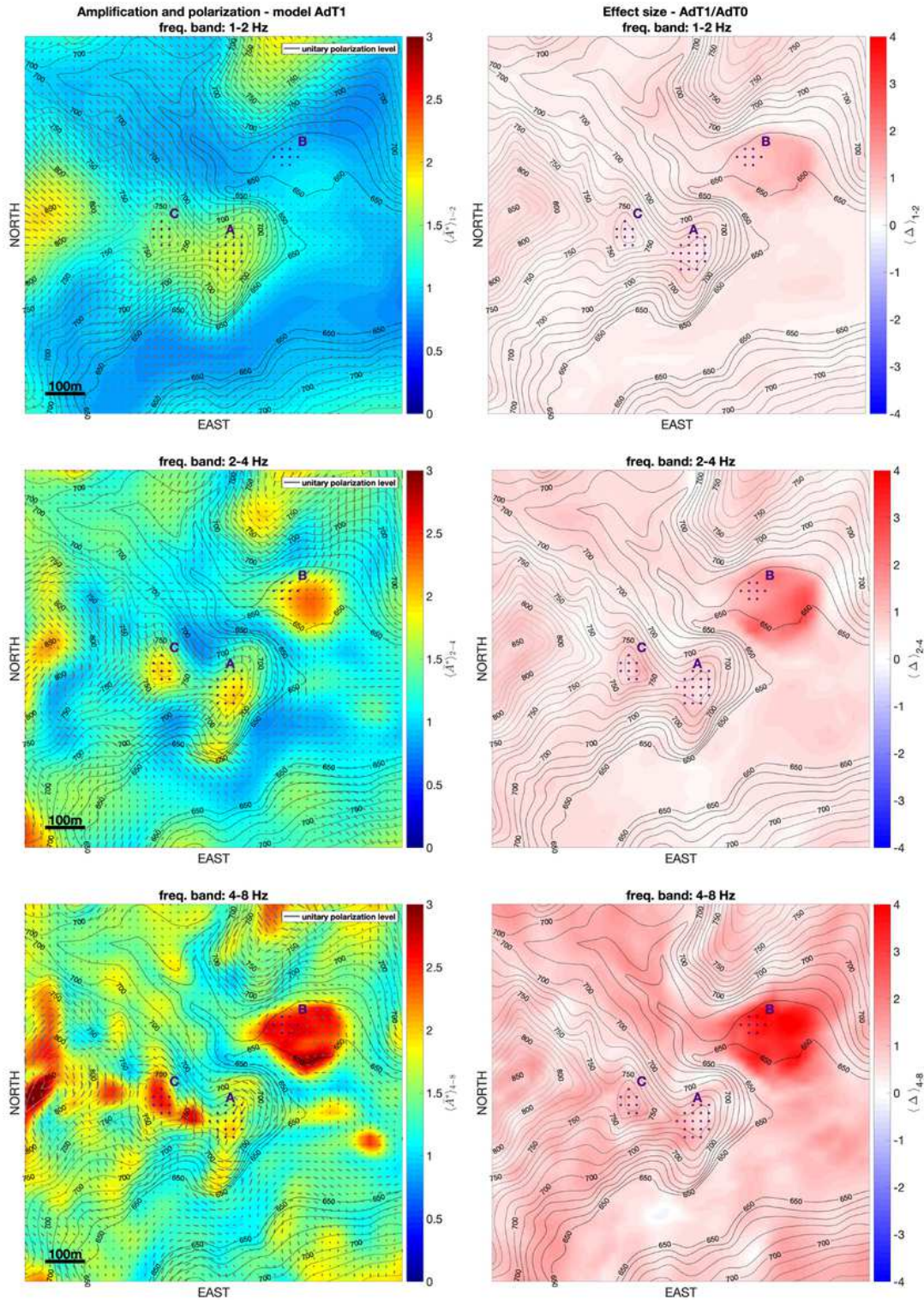


Figure 7

left) horizontal plane-wave amplification distribution pattern at Arquata del Tronto computed for the model AdT1 and in the frequency bands 1-2Hz, 2-4Hz and 4-8Hz. Same notation as in Fig.4; right) the

effect size (see Eq. 17 in the text) in the amplification values for the model AdT1 in respect to model AdT0

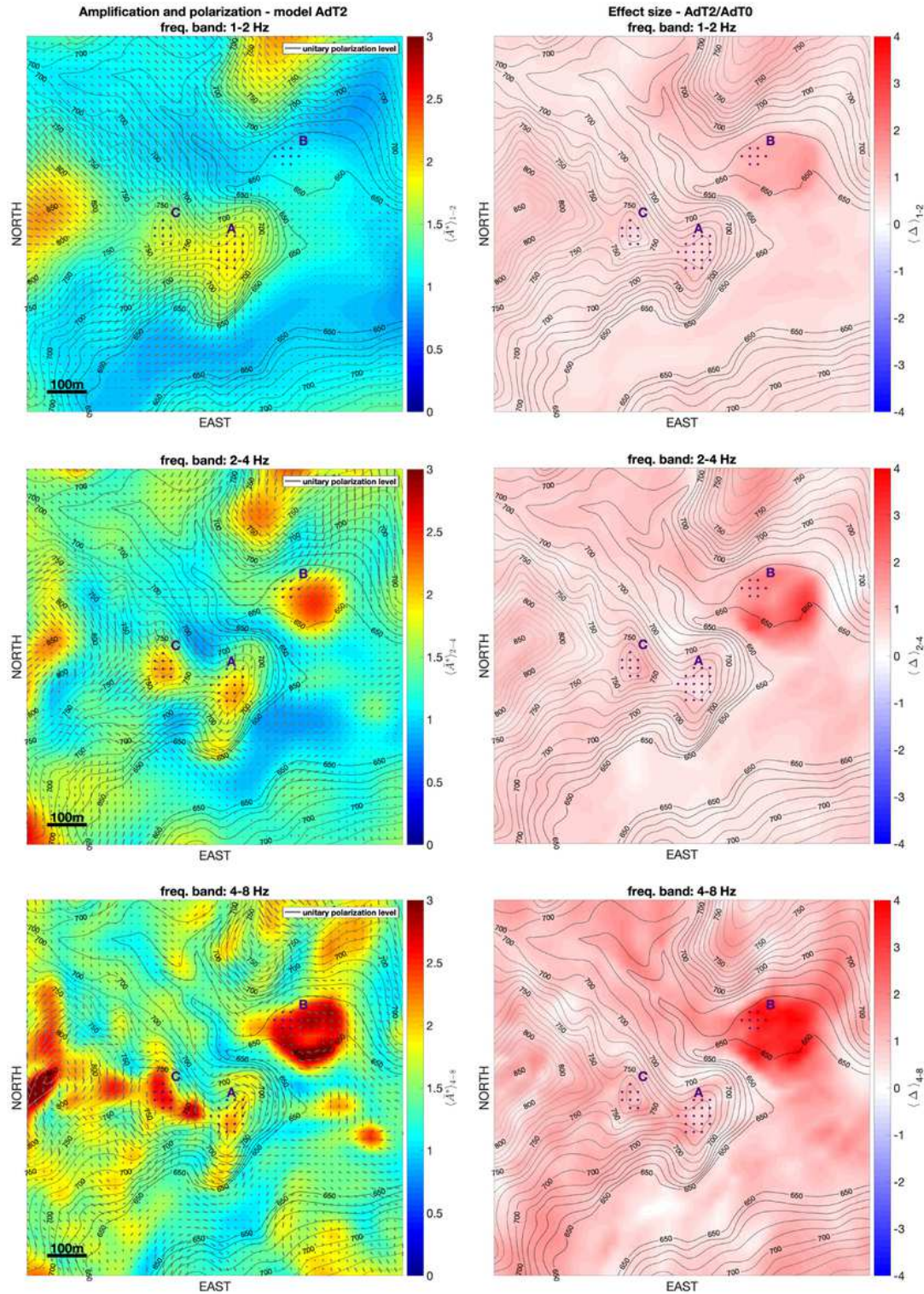


Figure 8

left) horizontal plane-wave amplification distribution pattern at Arquata del Tronto computed for the model AdT2 and in the frequency bands 1-2Hz, 2-4Hz and 4-8Hz. Same notation as in Fig.4; right) the

effect size (see Eq. 17 in the text) in the amplification values for the model AdT2 in respect to model AdT0

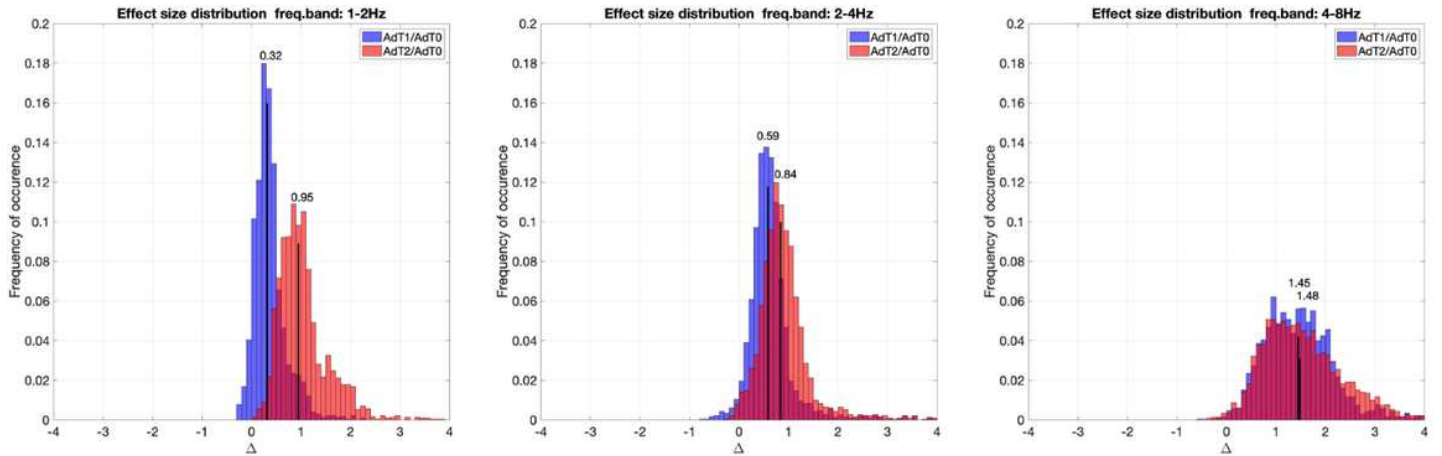


Figure 9

histograms of the amplification effect size values over the grid points sampling the studied area for the frequency bands: 1-2Hz, 2-4Hz and 4-8Hz. The median value is indicated in order to assess the overall differences between the changes in the amplification functions due to the variations in the structural models

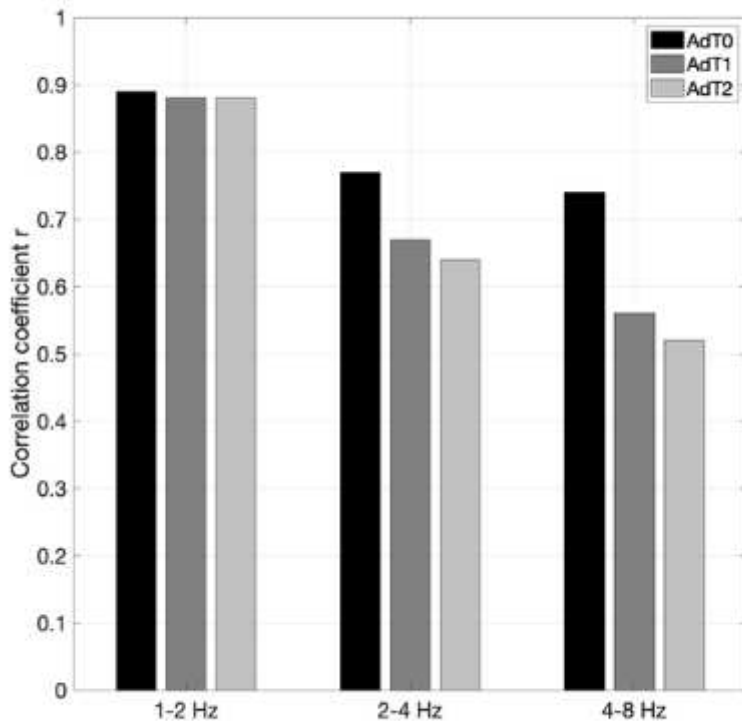
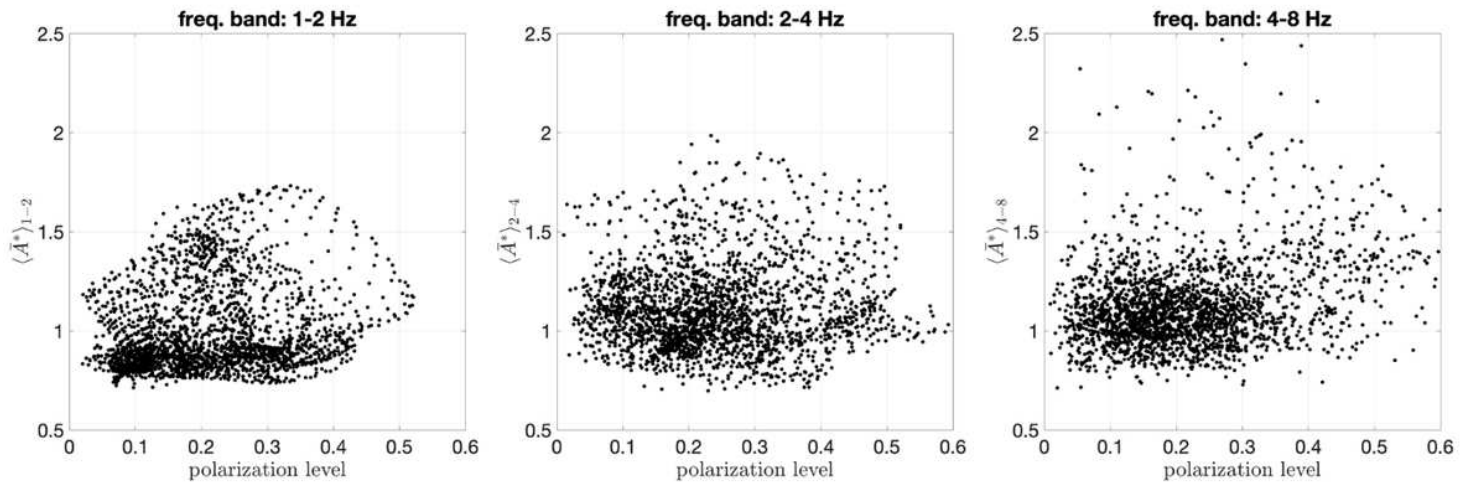


Figure 10

correlation coefficients between averaged horizontal plane-wave amplification and smoothed curvature obtained in the three frequency bands of interest for homogeneous model AdT0 (black), inhomogeneous model AdT1 (dark grey) and 3D model AdT2 (light grey)



**Figure 11**

distribution of amplification values in function of the polarization level in the three frequency bands for the Model AdT0 case

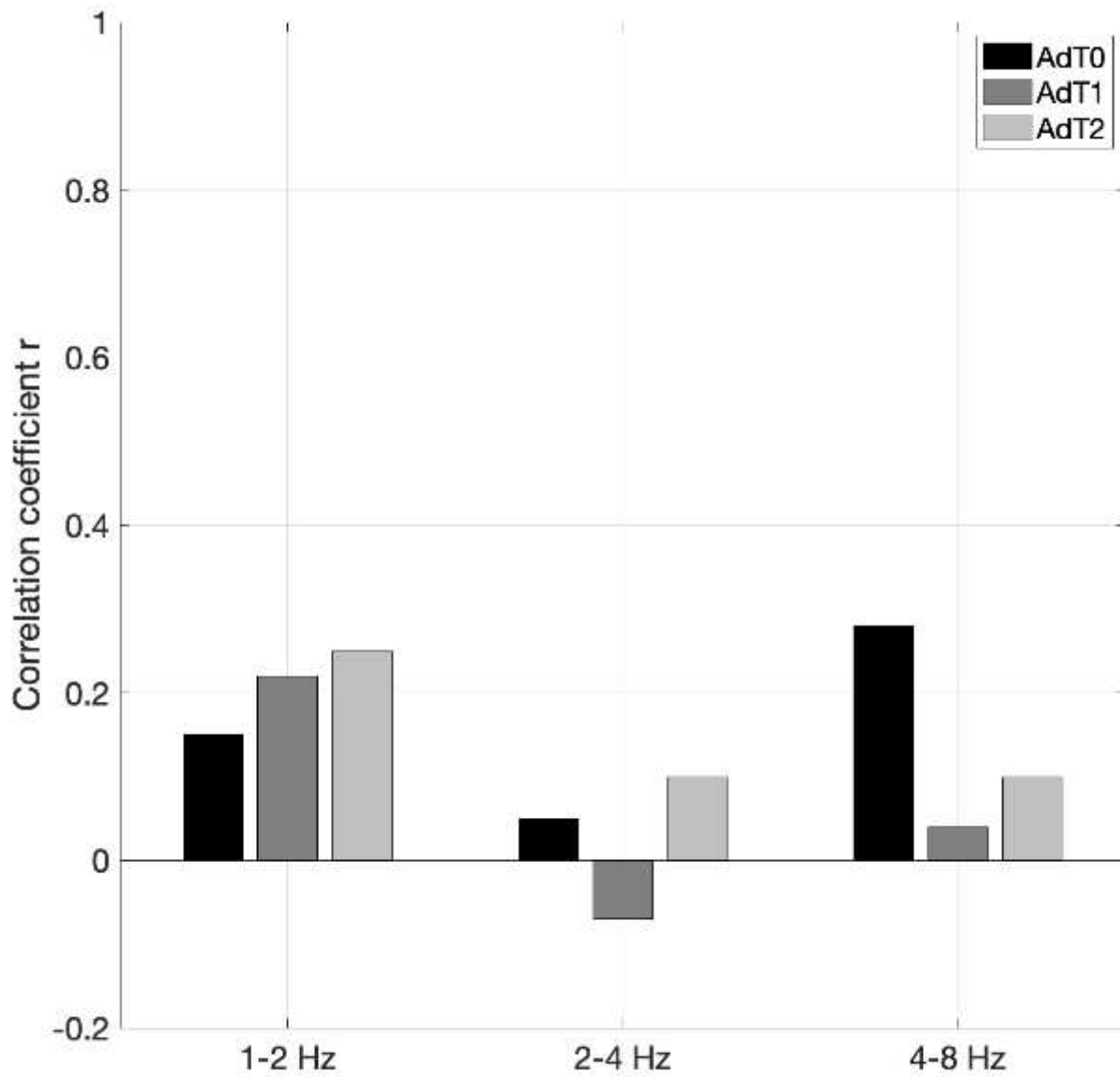


Figure 12

the values of the linear correlation coefficient between the polarization level and amplification

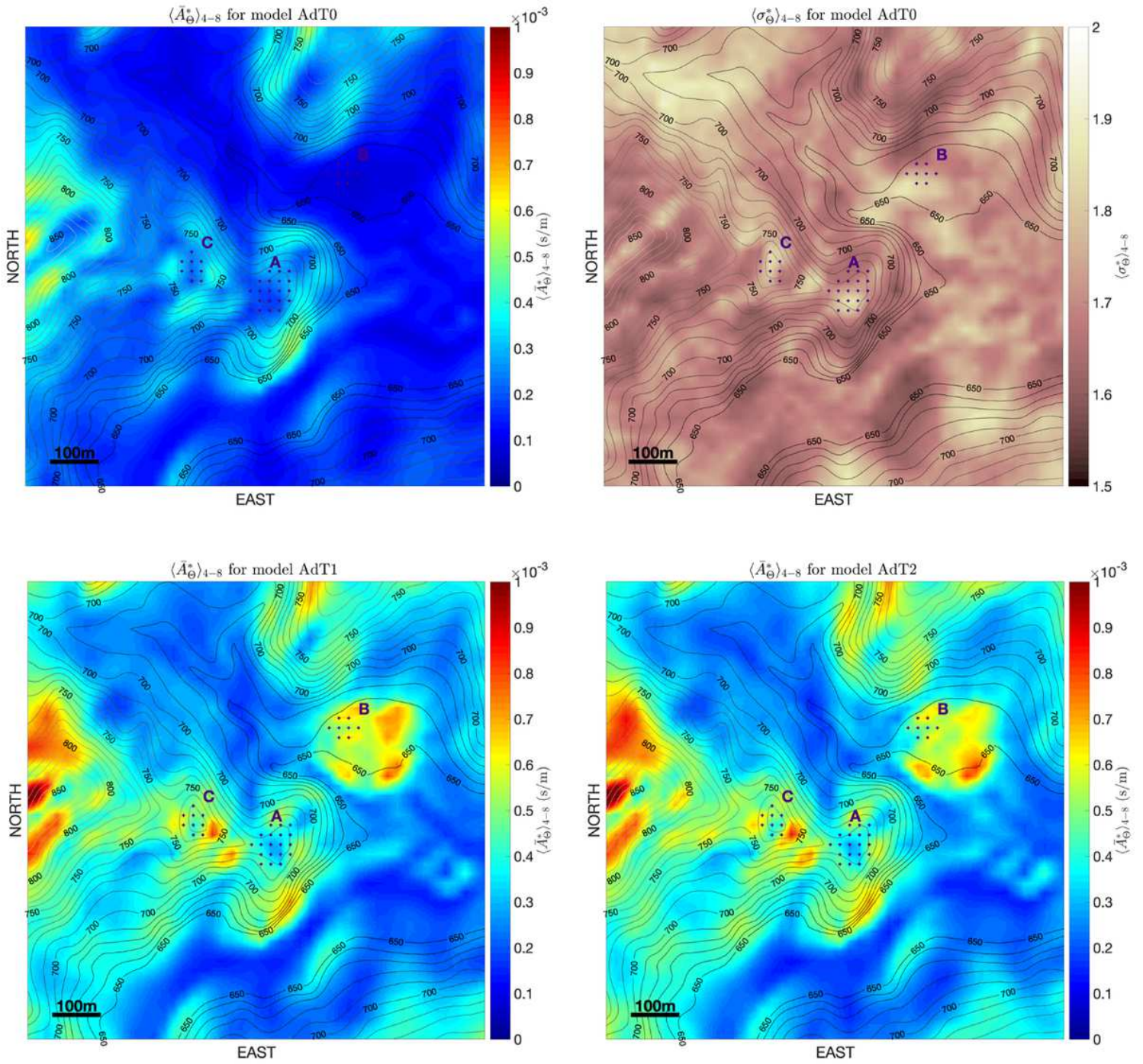
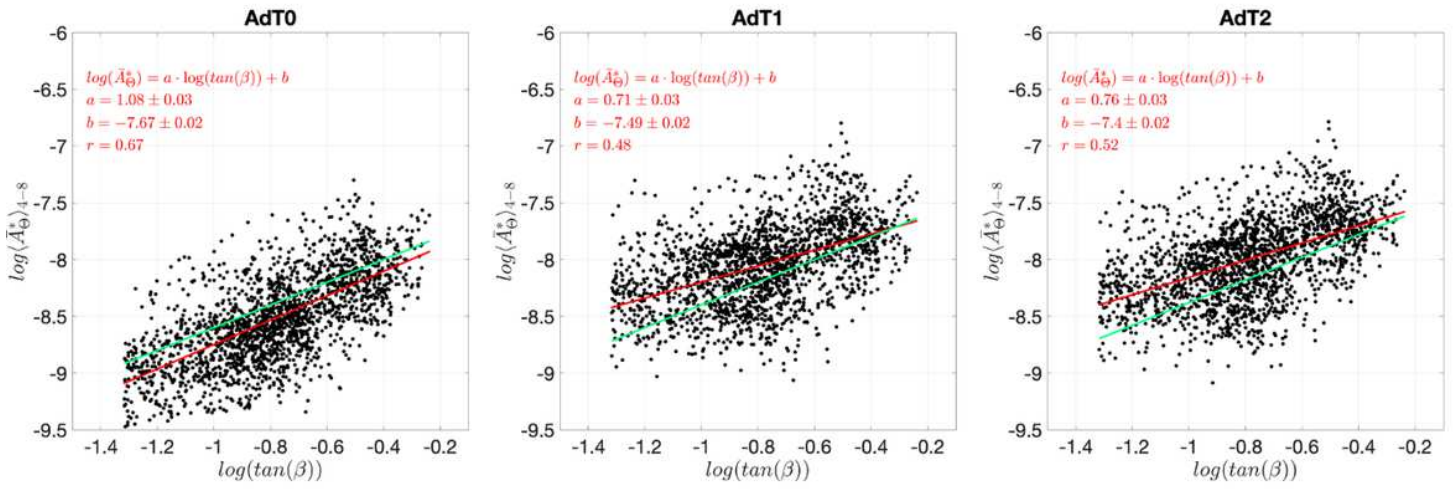


Figure 13

Please see the Manuscript PDF file for the complete figure caption.



**Figure 14**

Please see the Manuscript PDF file for the complete figure caption.

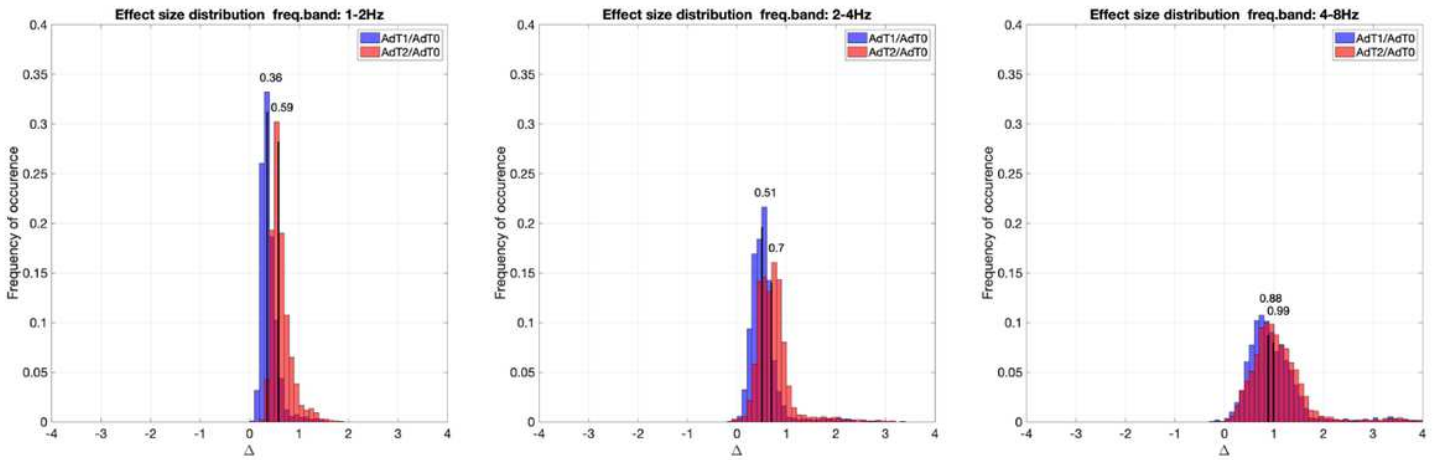


**Figure 15**

Please see the Manuscript PDF file for the complete figure caption.